DISSERTATIONS IN
FORESTRY AND
NATURAL SCIENCES

Ville Rimpiläinen

Electrical tomography imaging in pharmaceutical processes

Publications of the University of Eastern Finland
Dissertations in Forestry and Natural Sciences

UNIVERSITY OF
EASTERN FINLAND

VILLE RIMPILÄINEN

Electrical tomography imaging in pharmaceutical processes

Publications of the University of Eastern Finland
Dissertations in Forestry and Natural Sciences
No 68

Academic Dissertation
To be presented by permission of the Faculty of Science and Forestry for public examination in the Auditorium L22 in Snellmania Building at the University of Eastern Finland, Kuopio, on May, 18, 2012,
at 12 o'clock noon.

Department of Applied Physics

Kopijyvä Oy
Kuopio, 2012
Editor: Profs. Pertti Pasanen and Pekka Kilpeläinen

Distribution:
University of Eastern Finland Library / Sales of publications
P.O. Box 107, FI-80101 Joensuu, Finland
tel. +358-50-3058396
http://www.uef.fi/kirjasto

ISBN: 978-952-61-0777-6 (printed)
ISSNL: 1798-5668
ISSN: 1798-5668
ISBN: 978-952-61-0778-3 (pdf)
ISSN: 1798-5676

Author's address:
University of Eastern Finland
Department of Applied Physics
P.O.Box 1627
FI-70211 KUOPIO
FINLAND
email: ville.rimpilainen@uef.fi

Supervisors:
Lasse M. Heikkinen, Ph.D.
University of Eastern Finland
Department of Applied Physics
P.O.Box 1627
FI-70211 KUOPIO
FINLAND
email: lasse.heikkinen@uef.fi

Professor Marko Vauhkonen, Ph.D.
University of Eastern Finland
Department of Applied Physics
email: marko.vauhkonen@uef.fi

Arto Voutilainen, Ph.D.
University of Eastern Finland
Department of Applied Physics
email: arto.voutilainen@uef.fi

Reviewers:
Professor Kyung Youn Kim, Ph.D.
Jeju National University
Department of Electronic Engineering
Ara 1-Dong
JEJU 690 756
REPUBLIC OF KOREA
email: kyungyk@jejunu.ac.kr

Docent Lubomir Gradinarsky, Ph.D.
AstraZeneca R&D, Mölndal
Pepparedsleden 1
SE-431 83 MÖLNDAL
SWEDEN
email: lubomir.gradinarsky@astrazeneca.com

Opponent:
Associate Professor František Štěpánek, Ph.D.
Institute of Chemical Technology, Prague
Department of Chemical Engineering
Technická 5
CZ-166 28 PRAGUE
CZECH REPUBLIC
email: frantisek.stepanek@vscht.cz

ABSTRACT

In the pharmaceutical industry, the measurement techniques that are normally used to monitor manufacturing processes can sometimes be inadequate. For example, sampling methods are often slow and cumbersome, and methods based on point measurements can be unrepresentative. Therefore, there is a need for more comprehensive measurement techniques, such as electrical tomography imaging.

In this thesis, electrical capacitance tomography (ECT) and electrical impedance tomography (EIT) have been applied in monitoring of three common pharmaceutical unit processes. In electrical tomography, a set of electrodes is attached onto the surface of the object under study, electrical measurements are carried out through the electrodes, and tomograms that illustrate the electrical properties of the interior are reconstructed with the help of the measured data and mathematical algorithms.

In the first study, ECT was used to monitor high-shear granulation of pharmaceutical powders. In high-shear granulation, powders are built up into granules with the help of high-speed impeller blades and liquid addition. In the second study, fluidized-bed drying of pharmaceutical granules was monitored with ECT. In fluidized-bed drying, wet granules are dried with the help of a heated stream of air. In the third study, dissolution testing of pharmaceutical tablets was monitored with EIT. The testing is carried out to study and develop the drug release properties of solid dosage forms and to assure adequate batch-to-batch consistency in manufacturing.

In this thesis, various technical means about how to implement the imaging modalities to monitor these processes have been described, the applicability of the imaging modalities has been verified with realistic materials and experimental conditions, and signals for process monitoring purposes have been generated with the help of the reconstructed tomograms. It is concluded that ECT and EIT are versatile imaging modalities that can be applied for diverse

processes with the help of appropriate technical and computational customization.

Universal Decimal Classification: 621.317.33, 621.317.73
National Library of Medicine Classification: WN 206, QV 778
PACS Classification: 84.37.+q, 87.63.Pn
INSPEC Thesaurus: process monitoring; manufacturing processes; pharmaceutical industry; capacitance; capacitance measurement; tomography; electric impedance; electric impedance measurement; electric impedance imaging; granular materials; powders; drying; fluidised beds; dissolving
Yleinen suomalainen asiasanasto: prosessit; monitorointi; tarkkailu; lketeollisuus; kapasitanssitomografia; impedanssitomografia; rakeistus; kuivaus; liuotus

Acknowledgments

The work was carried out mainly at the Department of Applied Physics and at the School of Pharmacy of the University of Eastern Finland (previously University of Kuopio) during the years 2007–2012.

I am very grateful to my main supervisor Lasse M. Heikkinen, PhD, and Professor Marko Vauhkonen, PhD, for their valuable guidance and encouragement during the years. I also want to thank my other supervisors Arto Voutilainen, PhD, and Anssi Lehikoinen, MSc (tech.), for their guidance and for the fruitful discussions. In addition, I thank Professor Jari P. Kaipio, PhD, for originally employing me.

I thank the official reviewers Professor Kyung Youn Kim, PhD, and Docent Lubomir Gradinarsky, PhD, for the assessment of the thesis. In addition, I thank Ewen MacDonald, PhD, for the linguistic revisions.

I thank the staff of the Department of Applied Physics and the School of Pharmacy, it has been a great pleasure to work with all of you. Especially, I want to thank Marko Kuosmanen, MSc, Sami Poutiainen, MSc, Tuomo Savolainen, PhD, Professor Kristiina Järvinen, PhD, and Professor Jarkko Ketolainen, PhD, who have been the co-authors in the papers. I thank Professor Ketolainen also for his comments on the first chapter of the thesis. Furthermore, I thank Jari Kourunen, MSc, and Mr. Aimo Tiihonen for their help with the measurement equipment. I thank my previous roommates, especially Teemu Luostari, MSc, Jussi Toivanen, MSc, and Ossi Lehtikangas, MSc, for all the scientific and particularly the not-so-scientific discussions. Last but not least, I thank Kimmo Karhunen, MSc, Antti Nissinen, PhD, Antti Lipponen, MSc, and Gerardo del Muro González, MSc, for their friendship and support.

One part of the work was carried out in Canada in the Univer-

sity of Saskatchewan. I thank Professor Todd Pugsley, PhD, PEng, and the members of the FLASK research group for their hospitality during my visit. Especially, I thank Kurt Woytiuk, MSc, David Sanscartier, PhD, Regan Gerspacher, MSc, Francisco Sanchez, MSc, and Mohammad Omer Choudhary, MSc, for their friendship and the valuable advice.

I thank my parents Vilho and Anna, my sister Tarja and my brother Jouni including their families and all my friends for their support and encouragement.

Promis Centre consortium is thanked for providing research facilities. All the financial supporters are gratefully acknowledged: the Finnish Funding Agency for Technology and Innovation (TEKES), the collaborating companies in VARMA, PAT KIVA and PROMET projects, The Finnish Cultural Foundation and The Graduate School of Inverse Problems.

Kuopio April 22, 2012 *Ville Rimpiläinen*

ABBREVIATIONS

1D	One-dimensional
2D	Two-dimensional
3D	Three-dimensional
API	Active pharmaceutical ingredient
CFD	Computational fluid dynamics
ECT	Electrical capacitance tomography
EIDORS	Electrical impedance tomography and diffuse optical tomography reconstruction software
EIT	Electrical impedance tomography
EMA	European Medicines Agency (previously EMEA)
ERT	Electrical resistance tomography
FDA	United States Food and Drug Administration
FEM	Finite element method
FFT	Fast Fourier transform
MCC	Microcrystalline cellulose
MIT	Magnetic induction tomography
NIR	Near infra-red
PAT	Process analytical technology
PCA	Principal component analysis
PCB	Printed circuit board
PID	Proportional intergral derivative
PVP	Polyvinylpyrrolidone
USP	United States Pharmacopoeia
UV	Ultraviolet
VIS	Visible light

NOMENCLATURE

$\boldsymbol{B}$	Magnetic field
C	Capacitance (measured)
c	Drug concentration
$c_t(\boldsymbol{x})$	Drug concentration distribution at time point t
$\boldsymbol{D}$	Electric displacement field
$\boldsymbol{E}$	Electric field
e_{ex}	Surface of the excitation electrode
e_l	Surface of the lth electrode
f_1	Difference factor
$\boldsymbol{H}$	Magnetic field intensity
I	Electric current
i	Imaginary unit
$\boldsymbol{J}$	Jacobian matrix
$\boldsymbol{J}_z$	Jacobian matrix with respect to contact impedances
$\boldsymbol{j}$	Electric current density
$\boldsymbol{K}$	Reconstruction matrix
$\boldsymbol{L}$	Regularization matrix
$\boldsymbol{L}_z$	Regularization matrix for contact impedances
m	Number of measurements
m_t	Mass of the released drug at time point t
N	Number of discretization points
N_s	Number of samples taken during dissolution testing
N_e	Number of electrodes
n	Number of discretization points
Q	Electric charge (measured)
$\boldsymbol{Q}$	Set of measured electric charges
$\boldsymbol{Q}_{\text{ref}}$	Set of measured reference charges
q	Electric charge (computed)
$\boldsymbol{q}$	Set of computed electric charges
t	Time
U	Voltage (computed)
$\boldsymbol{U}$	Set of computed voltages
u	Electric scalar potential
$\boldsymbol{u}$, $u_h(\boldsymbol{x})$	Potential distribution
V	Excitation voltage

$\boldsymbol{V}$	Set of measured voltages
$\boldsymbol{V}_{\text{ref}}$	Set of measured reference voltages
v_{dist}	Superficial gas velocity (at the distributor level)
$\boldsymbol{v}_q$	Noise in charge measurements
$\boldsymbol{v}_{q,\text{ref}}$	Noise in reference charge measurements
$\boldsymbol{v}_v$	Noise in voltage measurements
$\boldsymbol{x}$	Spatial coordinate vector
z	Contact impedance
$\boldsymbol{z}$	Set of contact impedances
$\boldsymbol{z}_{\text{ref}}$	Set of reference contact impedances
α	Regularization parameter
α_z	Regularization parameter for contact impedances
$\delta\boldsymbol{v}_q$	Difference of noise terms
ϵ	Permittivity
$\boldsymbol{\epsilon}$, $\epsilon(\boldsymbol{x})$	Permittivity distribution
$\boldsymbol{\epsilon}_{\text{lin}}$	Permittivity distribution at linearization point
$\boldsymbol{\epsilon}_{\text{pr}}$	Prior assumption for the permittivity distribution
ϵ_r	Relative permittivity
$\boldsymbol{\epsilon}_{\text{ref}}$	Reference permittivity distribution
ϵ_{vac}	Vacuum permittivity, 8.8542×10^{-12} Fm^{-1}
$\boldsymbol{\eta}$	Outward unit normal vector in EIT
κ	Step parameter
μ	Magnetic permeability
$\boldsymbol{\nu}$	Outward unit normal vector in ECT
ρ	Electric charge density
σ	Conductivity
$\boldsymbol{\sigma}$, $\sigma(\boldsymbol{x})$	Conductivity distribution
$\boldsymbol{\sigma}_{\text{pr}}$	Prior assumption for the conductivity distribution
$\boldsymbol{\sigma}_{\text{ref}}$	Reference conductivity distribution
ϕ, φ	Basis function in FEM
χ	Moisture content
Ω	Domain
Ω_{e_l}	Volume that covers the lth electrode
$\partial\Omega$	Boundary of the domain
$\partial\Omega_{\text{sc}}$	Boundary of the screens
ω	Angular frequency

LIST OF PUBLICATIONS

This thesis consists an overview and the following four original publications which are referred to in the text by their Roman numerals:

I V. Rimpiläinen, S. Poutiainen, L. M. Heikkinen, T. Savolainen, M. Vauhkonen and J. Ketolainen, "Electrical capacitance tomography as a monitoring tool for high-shear mixing and granulation," *Chem. Eng. Sci.* **66,** 4090–4100 (2011).

II V. Rimpiläinen, L. M. Heikkinen and M. Vauhkonen, "Moisture distribution and hydrodynamics of wet granules during fluidized-bed drying characterized with volumetric electrical capacitance tomography," *Chem. Eng. Sci.* **75,** 220–234 (2012).

III V. Rimpiläinen, L. M. Heikkinen, M. Kuosmanen, A. Lehikoinen, A. Voutilainen, M. Vauhkonen and J. Ketolainen, "An electrical impedance tomography-based approach to monitor *in vitro* sodium chloride dissolution from pharmaceutical tablets," *Rev. Sci. Instrum.* **80,** 103706 (2009).

IV V. Rimpiläinen, M. Kuosmanen, J. Ketolainen, K. Järvinen, M. Vauhkonen and L. M. Heikkinen, "Electrical impedance tomography for three-dimensional drug release monitoring," *Eur. J. Pharm. Sci.* **41,** 407–413 (2010).

AUTHOR'S CONTRIBUTION

All publications are results of joint work with the supervisors and co-authors. Publications **I**, **II** and **IV** were principally written by the author, and the co-authors provided supervision and editorial guidance. Publication **III** was written by the author and Lasse M. Heikkinen, PhD.

The author implemented all the numerical computations using MatLab® and computed all the results in Publications **I-IV**. The two-dimensional ECT-codes used in Publication **I** were based on codes written by Lasse M. Heikkinen, PhD. The three-dimensional ECT-codes in Publication **II** were written by the author. Some of the codes used in computing the results in Publications **III** and **IV** such as the finite element solver for EIT have been previously developed in the Department of Applied Physics.

All the experiments were designed mainly by the author. The experimental work in Publication **I** was conducted in collaboration with Sami Poutiainen, MSc. and Tuomo Savolainen, PhD. The experimental work in Publication **II** was conducted by the author. The author conducted all the EIT-measurements in Publications **III-IV**; the tested tablets were made and the reference measurements with UV/VIS spectrophotometer were carried out by Marko Kuosmanen, MSc. The interpretations of the results and the conclusions were made principally by the author.

Contents

1 Introduction and background

At the beginning of the 21st century, it was realized in the pharmaceutical industry that it had lagged behind other areas of industry in its manufacturing techniques and especially in its process monitoring techniques. There were several reasons why this had occurred, but the most commonly mentioned reason was the strict regularization within the industry practised by the authorities which did not encourage to make any improvements [1–3]. Another reason that was quoted in [3] was that spending money in order to improve the manufacturing did not seem as good an investment as spending the same money in an effort to find a new medicine. However, since the research and development costs were increasing while the amount of new medicines per year entering the market was not [4], and in addition, since the generic drug companies started to compete with the traditional companies for the same group of consumers with lower prices, further savings in the manufacturing costs needed to be made.

At this point, the most important authority of the pharmaceutical industry, the U.S. Food and Drug Administration (FDA) woke up and released guidance for the industry which described the use of process analytical technology (PAT) as a framework for development, manufacturing and quality assurance [2]. Soon after that, the European Medicines Agency (EMA, previously EMEA) followed with a similar initiative. From the regulators' point of view, achieving more consistency and improvements in the quality (and thus also in the safety) of the drug products was seen as an important motivation to support PAT activities.

The FDA's guidance [2] considers *"PAT to be a system for designing, analyzing, and controlling manufacturing through timely mea-*

surements (i.e, during processing) of critical quality and performance attributes of raw and in-process materials and processes, with the goal of ensuring final product quality." In other words, the ultimate goal of PAT can be broken into three parts: (i) to identify the critical material and process attributes that affect the product quality, (ii) to understand how they affect the product quality, for example with the help of mathematical models, and finally (iii) to monitor these attributes and to control the process in real time (or near-real time) in order to assure the quality of the final product [2,5].

In this thesis, PAT is used as a guiding framework in the implementation of electrical tomography imaging techniques to monitor three unit processes commonly used in the pharmaceutical industry. The construction of adaptive process control loops is considered to be beyond the scope of this thesis.

1.1 OPERATIONAL PRINCIPLE OF ELECTRICAL TOMOGRAPHY

Most common materials can be regarded as either insulators or conductors based on their electrical properties. The insulators can be characterized based on their dielectric permittivity and the conductors on their electric conductivity. For bulk materials, these properties can be determined with the help of either capacitance or resistance measurements. In electrical tomography, this concept is taken one step further: the aim is to determine the *distribution* of these properties inside an object with the help of a series of electrical measurements made around the boundaries of the object.

The concept of electrical tomography consists of electrical capacitance tomography (ECT), electrical impedance tomography (EIT), electrical resistance tomography (ERT) and magnetic induction tomography (MIT). In this thesis, the first three techniques will be considered. The operational principle is as follows: first, a set of sensing electrodes is attached onto the surface of the object being studied, second, electrical boundary measurements are made through the electrodes, and third, the electrical properties inside

the object are reconstructed with the help of the measured data and mathematical algorithms. These steps are pictured in figure 1.1.

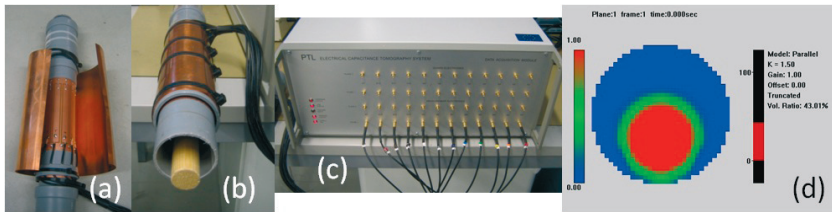

Figure 1.1: (a) A set of electrodes is patterned on a flexible copper-coated laminate and the laminate is attached around a plastic tube. The electrodes are covered with a copper shielding (or a screen) to diminish external noise. This piece of equipment is called an ECT sensor. (b) A piece of wood is placed inside the sensor. (c) An ECT measurement device measures capacitances through the coaxial cables that are connected to the electrodes. (d) With the help of the measured data and mathematical algorithms, a tomogram that represents the permittivity distribution inside the sensor is reconstructed. The ECT equipment and the software seen in the photographs are products of Process Tomography Ltd.

ECT is commonly used when the studied object consists of insulating media and ERT when the object consists of conductive media. In EIT, both kinds of media can be present. It is noteworthy that in the literature, EIT and ERT are often regarded as the same modality. This is partly a naming convention and partly because there are only few EIT measurement systems that can provide the measurement data that is needed in order to reconstruct both conductivity and permittivity distributions; usually only the conductivity distribution is reconstructed, thus the modality in question is actually ERT.

1.2 UNIT PROCESSES IN THE PHARMACEUTICAL INDUSTRY

At the moment, the pharmacetical industry is heavily batch-oriented in terms of its manufacturing techniques. There are manufacturing processes for two purposes: first to synthesize active pharmaceutical ingredients (APIs) and second to manufacture different dosage forms (these are also called the primary and secondary manufactur-

ing, respectively). The PAT concept is mainly intended for processes utilizing the latter purpose [3]. Figure 1.2 shows one possible chain of unit processes (or unit operations) that are needed to produce pharmaceutical products. The end product of the chain is typically a tablet.

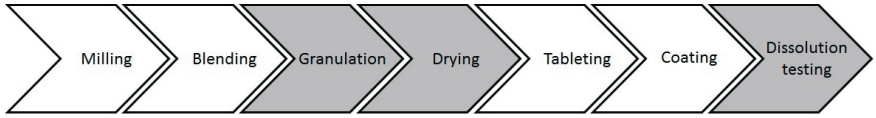

Figure 1.2: A possible chain of unit processes for manufacturing pharmaceutical tablets. The unit processes that are colored with gray are the ones that are studied in this thesis.

The raw materials in tablet manufacturing are often powders. In addition to API, the materials may include fillers, binders and disintegrants. At the start, the raw materials are milled if they are not yet in a suitable powder form. In the blending process, the powder mixture is homogenized. The powder blend can next be compressed directly into a tablet; however, often granulation precedes this process.

In the granulation process, the powders are enlarged into granules. Granules are preferred because they flow better, are easier to process, do not cause dust -related problems and sometimes can provide better drug content uniformity. Wet granulation [6–9] is one of the methods which can be used to form granules and it can be carried out in a high- or low-shear granulator, a fluidized-bed granulator or a drum granulator. Other common methods are dry granulation in a roll compactor [10] and melt granulation in either a high-shear mixer [11] or a fluidized-bed granulator [12].

After wet granulation, the granules need to be dried. Drying of granular materials is usually carried out in a fluidized-bed dryer [13,14] or a tray dryer. Tabletting is usually achieved through compaction [15,16]. An optional step is coating of the tablets' surface which can be used to fine tune the drug release properties or to improve preservation during storage. Finally, dissolution testing [17] is carried out on a sample set of the end-product batch to

ensure adequate drug release properties and batch-to-batch consistency.

Recently, much attention has been paid to continuous processing because it can further improve the product quality and reduce the costs [18]. It is worth noting, that also the FDA's PAT guidance for industry mentions continuous processing as one of the means to *"improve efficiency and manage variability"* [2].

In this thesis, three unit processes have been studied with electrical tomography imaging: the granulation process in a high-shear mixer, the drying process in a fluidized-bed dryer and the dissolution testing in USP apparatus II.

1.2.1 High-shear granulation

In high-shear wet granulation, powder particles are built up into granules with the help of high speed impeller blades and liquid addition. The liquid binds the powder particles together, and the blades are needed for mixing the material and breaking up big agglomerates (see figure 1.3). There are different kinds of high-shear granulators with variations in the number, size and shape of the mixing blades. A laboratory -scale high-shear mixer is presented in figure 1.4.

The adjustable process parameters include impeller speed, liquid addition method/rate and processing time. In addition, there are parameters that are usually kept fixed during the process such as the type of impeller, the compositions and total amount of raw materials. Even minor changes in the adjustable process parameters can affect the outcome. Usually, the objective is to produce granules with a consistent particle size distibution.

Traditionally, the torque and power consumption of the mixer have been used as measures of the phase of the granulation process [19,20]. Recently, near infra-red (NIR) detectors [21,22], acoustic emission spectra [23], image processing [24] and microwave measurements [25] have been applied for in-line monitoring. However, until now electrical tomography techniques have not been used for

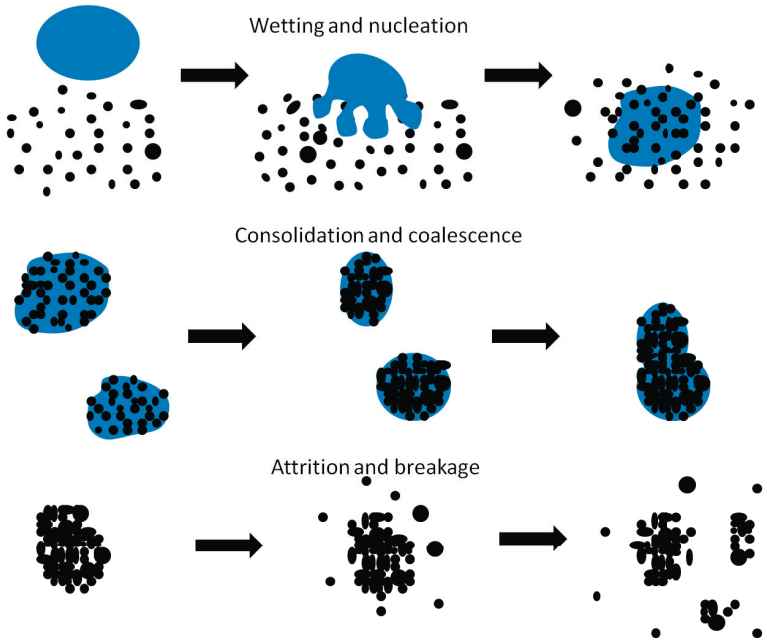

Figure 1.3: According to [6], granulation is characterized with the help of three rate processes: wetting and nucleation (top row), consolidation and coalescence (middle row) and attrition and breakage (bottom row).

this purpose.

1.2.2 Fluidized-bed drying

The drying of the wet granules is usually performed in a fluidized-bed dryer. In the dryer, moisture is transferred from the wet granules to a heated stream of air that is injected through the material. Fluidized-beds are usually either cylindrical or conical in shape. A laboratory scale fluidized-bed is shown in figure 1.5.

The adjustable process parameters are the humidity, temperature and velocity of the fluidizing air and processing time. The objective is to obtain granules with a desired moisture content. Furthermore, hydrodynamics (or fluid dynamics) has an effect on the particle size distribution, and since the hydrodynamics change as the granules dry, it is preferable to be able to adjust the hydrody-

Figure 1.4: A laboratory -scale high-shear granulator.

namics during the process.

Traditionally the temperature and humidity of the outlet air has been used in monitoring of fluidized-bed drying. Other methods include NIR detectors [26], microwave resonance technology [27] and triboelectric probes [28]. The hydrodynamics of fluidized-beds is usually assessed with the help of pressure measurements. Pressure measurements have also been used in a few studies to investigate the hydrodynamical conditions during drying [29–33]. In addition, ECT has previously been used in monitoring of the process, this will be further discussed in section 1.4.3.

1.2.3 Dissolution testing

Dissolution testing is used to investigate drug release from tablets, and it is a tool applied in tablet development, and a quality control method to demonstrate adequate batch-to-batch reproducibility. The testing methods need to be approved by the official regulatory authorities, and one of the most commonly used methods

Figure 1.5: A laboratory -scale fluidized-bed reactor.

is the United States Pharmacopoeia (USP) defined USP dissolution apparatus II.

In the USP II method, a tablet is inserted into a standardized vessel that is normally filled with 500 – 1000 ml of buffer solution. The buffer solutions imitate the pH and the temperature of gastric or intestinal fluids. A USP defined paddle rotates inside the vessel at a constant rate, usually in the range of 50–100 rpm. A photograph of the apparatus is presented in figure 1.6.

The dissolution testing is monitored by measuring drug concentration from a certain location i.e. according to USP directions, this should be between the liquid surface and the top of the paddle and more than one centimeter from the edge of the vessel. There are different ways to perform the monitoring e.g. traditional cannula sampling and automated sippers combined with off-line analysis such as UV/VIS spectrophotometry or high performance liquid chromatography. In-line monitoring methods include fiber-optic probes [34,35], potentiometric sensors [36,37] and conductivity probes [38]. Electrical tomography techniques have not been previously used for this purpose.

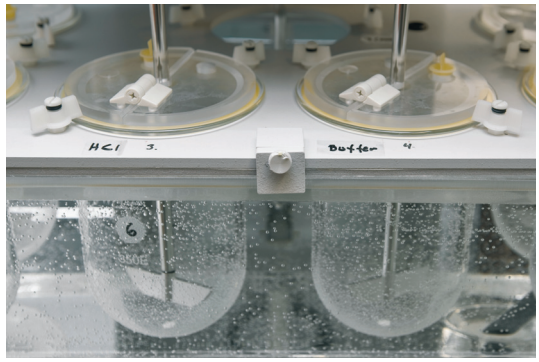

Figure 1.6: The USP dissolution apparatus II.

1.3 MOTIVATION FOR ELECTRICAL TOMOGRAPHY

One of the most versatile and common measurement technique used in in-line monitoring of pharmaceutical processes is NIR [39]. Other commonly used techniques are acoustic emission, microwave measurements and different probes utilizing electric measurements.

One can criticize the above mentioned techniques that they either measure processes in a pointwise manner (or from a relatively limited area) or by averaging the whole studied medium. Point measurements can be problematic: the results may depend strongly on the location of the sensor especially if inhomogenities are present; the number of possible installation locations is often limited; the installation of the sensor may require a hole being drilled into the processing vessel; and the sensor may need to be located inside the processing vessel which is not always feasible. Averaging the whole medium does not take into account any local inhomogenities nor the structure of the target. One further problem especially associated with NIR is the contamination of the observation window which can prevent the NIR measurements. Due to the above mentioned reasons, the presently used measurement techniques can sometimes be inadequate and that there is a need for more comprehensive monitoring tools.

Electrical tomography techniques are attractive alternatives to overcome these drawbacks, since they are non-intrusive, non-invasive, and the monitoring can be carried out in-line. The non-intrusiveness and non-invasiveness are important for the pureness of the product. These properties are especially evident in ECT in which the measurement electrodes can be installed on the outer surface of the product bowl; in ERT and EIT, however, the electrodes usually need to have a galvanic connection to the target and are therefore installed on the inner surface of the bowl. Furthermore, in-line monitoring is required to be able to control the processes in real time. The required monitoring signals are often relatively easy to obtain.

Electrical tomography imaging can be more comprehensive in

the sense that it provides both local and global information from the processes. The result of the measurements is usually either a two-dimensional (2D) or three-dimensional (3D) tomogram which describes the electrical properties of the target, and it can be used to detect local differences or to calculate characteristic numbers that describe the whole target.

Electrical tomography techniques are versatile monitoring tools, and they have previously been found useful, for example, in monitoring of mixing [40–45], separation [43, 44, 46–48], multi-phase flows [43, 49–54] and transportation [43, 51, 55]. Other uses include medical [56–58] and geophysical applications [59–61] and non-destructive testing [62].

1.4 LITERATURE REVIEW

This section reviews how pharmaceutical processes have previously been studied with electrical tomography.

1.4.1 Manufacturing processes of APIs

Ricard *et. al.* have described the use of ERT in several API manufacturing processes [44, 63]. They presented a glass reactor suitable for ERT measurements and accommodating different pharmaceutical processes [63]. ERT was used to monitor the *hydrolysis* of ethyl acetate in the reactor, and it was found that the conductivity decreased as the hydrolysis proceeded. The results were successfully compared with Raman spectroscopy measurements and modelling results.

In [44] a chemically compatible linear ERT sensor was used for measurements in two different lab-scale vessels. The experiments included monitoring of paracetamol *crystallization*. The crystallization process was carried out by cooling, and therefore the relationships between temperature, concentration and conductivity had to be first established. In the crystallization experiment, it was found that the conductivity decreased as the process proceeded, and the

conductivity curve bore strong resemblance to the particle count curve that was monitored with a reference method. In addition, it was found that ERT could be used to monitor phase dispersion and phase separation in liquid-liquid processes.

1.4.2 Fluidized-bed granulation

Two granulation processes with different batch size were monitored with ECT in [64]. It was noted that the distribution of solids and hydrodynamic properties change during the granulation. Furthermore, sticking of wet material to the walls could be seen in the capacitance data, and the frequency spectra computed with fast Fourier transform (FFT) displayed differences as a function of time.

1.4.3 Fluidized-bed drying

ECT has previously been used to study fluidized-bed drying in few studies by two groups. First, Professor Pugsley's group related the capacitance data from a packed bed of wet granules with moisture, and compared the radial density profiles determined from 2D-ECT and X-ray tomograms [65]. Subsequently, S-statistic analyses of ECT data and 2D-tomograms were used to interpret the hydrodynamic changes occurring during drying [66].

Professor Yang's group compared results from mathematical models, computational fluid dynamics (CFD) simulations and ECT measurements; associated capacitance measurements from a packed bed and during minimum fluidization of wet granules with moisture; and presented 2D-tomograms of the distribution of solids [67]. 2D-tomograms and frequency spectra computed with FFT were presented in [64]. They demonstrated an online method for controlling air flow rate during drying based on ECT measurements and a mathematical model [68]. They also investigated the effects of the excitation signal frequency and the data normalization method to the ECT results [69].

The reasons why fluidized-bed drying was chosen here as one of the processes to be studied, even though it had already been used

for that purpose, was that all the previous studies had been carried out using 2D-tomography and without taking the conical geometry of the product bowl into account. The utilization of 3D-tomography and the correct geometry are essential due to the fact that in such a chaotic process as fluidized-bed drying, one can hardly assume that the material distribution would be homogeneous in a vertical direction as is required for 2D-tomography, or that the varying diameter of the conical product bowl would not have any effect on the material distribution.

1.4.4 Fluidized-bed coating

Microcrystalline cellulose (MCC) particle concentration was studied during a coating process using ECT in [70]. 2D-tomograms, spatial mean concentration and fluctuations in the mean concentration were presented as a function of time. Based on the results, it was concluded that clusters were formed frequently during the first half of the process and rarely during the second half. Furthermore, particle movement was analyzed based on wavelet multi-resolution technique.

1.5 AIMS

In this thesis, three unit processes were investigated with electrical tomography. In each study, the aim was to generate signals from the tomograms that could be utilized for process monitoring. Various technical steps were needed first to implement the electrical imaging modalities. In addition, an effort was made to use realistic materials and relevant experimental conditions in all the studies. In the following, these aims and steps will be described in greater detail.

In the first study (Publication **I**), electrical capacitance tomography was used for monitoring the high-shear granulation. ECT was selected here because the used powders were insulating, even though at the end of the granulation process, the wet granules could

also have had electrically conductive properties. The aim and the technical steps in this study were as follows:

AIM: to develop 2D-ECT so that it could be used to monitor the progress of high-shear granulation.

STEP 1: to design and build an ECT sensor that could be used as a product bowl in high-shear granulations.

STEP 2: to take the metallic shaft in the middle of the sensor into account in such way that the tomograms would not be deteriorated; normally there are no metal objects inside ECT sensors because they would distort the electric field that is used for measurements.

In the second study (Publication **II**), ECT was used for monitoring the fluidized-bed drying. ECT was selected because the mixture of air and wet granules was predominantly insulating; however, the wet granules could also have had some electrically conductive properties at the beginning of the experiments when they were in a packed-bed state. The aim and steps in this study were:

AIM: to develop 3D-ECT so that it could be used to monitor both the moisture content and hydrodynamics of wet granules during fluidized-bed drying.

STEP 1: to take the correct geometry of the conical product bowl into account by using three-dimensional ECT and the finite element method (FEM).

STEP 2: to convert the 2D-ECT monitoring equipment to produce 3D-tomograms by computational means; the used ECT equipment was originally designed to carry out the measurements that were needed for producing two separate 2D-tomograms.

STEP 3: to reconstruct 3D moisture distributions.

In the third study (Publications **III** and **IV**), electrical impedance tomography was used for monitoring drug release from tablets. EIT was selected because the dissolution vessel was filled with liquid that was customized for EIT measurements. The aim and the steps in this study were:

AIM: to develop 3D-EIT so that it could produce drug release and drug release rate curves during dissolution testing.

STEP 1: to modify the USP dissolution apparatus II so that it would be suitable for EIT measurements.

STEP 2: to choose the materials in such way that the release of the drug substance could be observed with EIT.

STEP 3: to take the rotating paddle and the changing contact impedances[1] during the drug release appropriately into account; usually there are no additional objects inside EIT sensors because they affect the measurements, and the contact impedances are kept constant.

STEP 4: to reconstruct 3D concentration distributions.

[1]The contact impedances are used to model the drop in the electric potential that occurs when electric current flows through an electrode surface into the studied object.

2 Theory of electrical tomography

In electrical tomography, the estimation of the distribution that characterizes electrical properties of the domain requires solving both the forward and inverse problems. The forward problem describes how the desired distribution is related to the measured quantities, and in the inverse problem the distribution is estimated based on boundary measurements. In this section, the forward and inverse problems of ECT and EIT are described. For reviews on ECT and EIT, see [51,71–73] and [51,56,74–76], respectively.

The derivation of both forward problems start from the macroscopic Maxwell equations [77] that are valid in the imaging domain $\boldsymbol{x} \in \Omega \subset \mathbb{R}^3$, $t \in \mathbb{R}$

$$\nabla \times \boldsymbol{E}(\boldsymbol{x},t) = -\frac{\partial \boldsymbol{B}(\boldsymbol{x},t)}{\partial t} \tag{2.1}$$

$$\nabla \times \boldsymbol{H}(\boldsymbol{x},t) = \boldsymbol{j}(\boldsymbol{x},t) + \frac{\partial \boldsymbol{D}(\boldsymbol{x},t)}{\partial t} \tag{2.2}$$

$$\nabla \cdot \boldsymbol{D}(\boldsymbol{x},t) = \rho(\boldsymbol{x},t) \tag{2.3}$$

$$\nabla \cdot \boldsymbol{B}(\boldsymbol{x},t) = 0\,. \tag{2.4}$$

Here, $\boldsymbol{E}(\boldsymbol{x},t)$ is the electric field, $\boldsymbol{B}(\boldsymbol{x},t)$ the magnetic field, $\boldsymbol{H}(\boldsymbol{x},t)$ the magnetic field intensity and $\boldsymbol{D}(\boldsymbol{x},t)$ the electric displacement field. Furthermore, $\boldsymbol{j}(\boldsymbol{x},t)$ is the electric current density, $\rho(\boldsymbol{x},t)$ is the electric charge density, $\boldsymbol{x} \in \Omega$ is the spatial coordinate vector and t is time. The mathematical notation $\nabla\times$ is the curl operator, $\nabla\cdot$ is the divergence operator and $\partial/\partial t$ is the time derivative.

The following relations apply if the medium is assumed to be

linear and isotropic

$$\boldsymbol{D}(\boldsymbol{x},t) = \epsilon(\boldsymbol{x})\boldsymbol{E}(\boldsymbol{x},t)\ , \tag{2.5}$$

$$\boldsymbol{B}(\boldsymbol{x},t) = \mu(\boldsymbol{x})\boldsymbol{H}(\boldsymbol{x},t)\ , \tag{2.6}$$

$$\boldsymbol{j}(\boldsymbol{x},t) = \sigma(\boldsymbol{x})\boldsymbol{E}(\boldsymbol{x},t)\ , \tag{2.7}$$

where $\epsilon(\boldsymbol{x})$ is the dielectric permittivity, $\mu(\boldsymbol{x})$ the magnetic permeability and $\sigma(\boldsymbol{x})$ the electric conductivity.

In the following forward problem formulations, the assumptions about the electrical properties of the studied media are made based on the imaging technique in question, and the assumptions about the excitation signals are made based on the corresponding signals that were used in the experiments.

In the inverse problem formulations, the *deterministic framework* has been utilized. A few alternative approaches will be described in section 2.3.

2.1 ELECTRICAL CAPACITANCE TOMOGRAPHY

2.1.1 Forward problem

In ECT, the studied medium is assumed to be essentially insulating i.e. the electrically conductive properties of the medium are assumed to be negligible ($\sigma(\boldsymbol{x}) \approx 0$). Furthermore, here it is assumed that the excitation signal is a potential signal which has a square wave form. In essence, this means that the fields are assumed to be constant and time independent during the excitation / measurement cycle. Now, the Maxwell equations can be rewritten

$$\nabla \times \boldsymbol{E}(\boldsymbol{x}) = 0 \tag{2.8}$$

$$\nabla \times \boldsymbol{H}(\boldsymbol{x}) = 0 \tag{2.9}$$

$$\nabla \cdot \boldsymbol{D}(\boldsymbol{x}) = \rho(\boldsymbol{x}) \tag{2.10}$$

$$\nabla \cdot \boldsymbol{B}(\boldsymbol{x}) = 0\ . \tag{2.11}$$

The domain Ω of a typical ECT sensor is depicted in figure 2.1. It consists of the region of interest, the measurement electrodes that

are mounted on the surface of an insulating wall, and the grounded screen(s). The electrically grounded outer-screen reduces the external noise and it is separated with an insulating layer (typically air) from the interior. There may also be grounded screens between the electrodes. If all these parts are taken into account in the forward model, the model is sometimes called *the complete sensor model* [78].

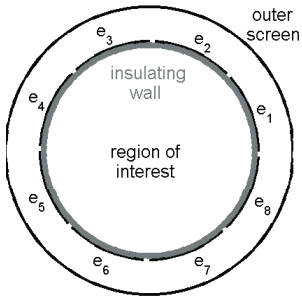

Figure 2.1: A typical ECT sensor consists of the region of interest, electrodes $(e_1, \cdots, e_8)$ *that are mounted on the surface of an insulating wall and the grounded outer-screen.*

In the forward problem, the electric potential distribution and the electric charges at the electrodes are solved with the help of the known excitation signals and the known permittivity distribution. The permittivity is defined as

$$\epsilon(\boldsymbol{x}) = \epsilon_{\text{vac}}\epsilon_r(\boldsymbol{x}), \tag{2.12}$$

where $\epsilon_{\text{vac}} \approx 8.8542 \times 10^{-12}$ Fm^{-1} is the vacuum permittivity and $\epsilon_r(\boldsymbol{x}) \geq 1$ is the relative permittivity of the medium.

The potential distribution is solved inside the domain Ω using the Poisson equation and suitable boundary conditions. The Poisson equation can be derived from equations (2.8) and (2.10) by first noting that since the curl of $\boldsymbol{E}(\boldsymbol{x})$ is zero, the electric field can be written in terms of an electric scalar potential $u(\boldsymbol{x})$ in the following way

$$\boldsymbol{E}(\boldsymbol{x}) = -\nabla u(\boldsymbol{x}), \tag{2.13}$$

where ∇ is the gradient operator. Since there are no free charges

inside the domain, the equation (2.10) can be written as

$$\nabla \cdot \boldsymbol{D}(\boldsymbol{x}) = 0 \,. \tag{2.14}$$

Now, by inserting the equations (2.5) and (2.13) in (2.14), the following result is obtained

$$\nabla \cdot \boldsymbol{D}(\boldsymbol{x}) = 0 \tag{2.15}$$

$$\Leftrightarrow \quad \nabla \cdot \epsilon(\boldsymbol{x}) \boldsymbol{E}(\boldsymbol{x}) = 0 \tag{2.16}$$

$$\Leftrightarrow \quad \nabla \cdot \epsilon(\boldsymbol{x}) \nabla u(\boldsymbol{x}) = 0 \,, \tag{2.17}$$

which is the Poisson equation. The boundary conditions for (2.17) depend on the measurement set-up, but usually the conditions are

$$u(\boldsymbol{x}) = 0, \quad \boldsymbol{x} \in \partial\Omega_{\text{sc}} \cup_{l=1}^{N_e} e_l \setminus e_{\text{ex}} \tag{2.18}$$

$$u(\boldsymbol{x}) = V, \quad \boldsymbol{x} \in e_{\text{ex}} \tag{2.19}$$

$$\epsilon(\boldsymbol{x}) \frac{\partial u(\boldsymbol{x})}{\partial \boldsymbol{\nu}} = 0, \quad \boldsymbol{x} \in \partial\Omega \setminus \left\{ \partial\Omega_{\text{sc}} \cup_{l=1}^{N_e} e_l \right\} \tag{2.20}$$

Here, $\partial\Omega$ is the boundary of the domain, $\partial\Omega_{\text{sc}}$ denotes the screens which are electrically grounded, e_l the surface of the lth electrode, N_e the number of electrodes, e_{ex} the surface of the excitation electrode, V is the excitation voltage, and $\partial u(\boldsymbol{x})/\partial \boldsymbol{\nu}$ is the derivative of the potential in the direction of the outward unit normal vector $\boldsymbol{\nu}$[1]. The condition (2.18) is valid at the sensing electrodes and at the electrically grounded boundaries, and the condition (2.19) is valid at the excitation electrode. The condition (2.20) is valid at the boundaries that are not made of metal and therefore are not at some specific potential, and the condition means that the electric displacement field is zero in the direction of the unit normal at the boundary.

Usually in ECT, the measured quantities are capacitances between electrodes. However, the measurements can also be formulated with respect to electric charges with the help of the relationship

$$Q = VC, \tag{2.21}$$

[1]Here the word "outward" means outwards from the electrode i.e. away from the electrode surface.

where Q denotes the electric charge, V excitation voltage and C capacitance. Electric charges can be more straightforward in cases where several electrodes are excited simultaneously.

Now, the electric charge of the lth electrode can be solved by integrating the equation (2.10) over the electrode volume Ω_{e_l}

$$\int_{\Omega_{e_l}} \nabla \cdot \boldsymbol{D}(\boldsymbol{x}) \mathrm{d}\boldsymbol{x} = \int_{\Omega_{e_l}} \rho(\boldsymbol{x}) \mathrm{d}\boldsymbol{x}. \tag{2.22}$$

The right-hand-side of the equation (2.22) is equal to the total electric charge q_l, and the left-hand-side can be transformed into a surface integral using the divergence theorem

$$\int_{e_l} \boldsymbol{D}(\boldsymbol{x}) \cdot \mathrm{d}\boldsymbol{S} = q_l. \tag{2.23}$$

This can be further modified into the form

$$\begin{aligned} q_l(\epsilon) &= \int_{e_l} \boldsymbol{D}(\boldsymbol{x}) \cdot \mathrm{d}\boldsymbol{S} && (2.24)\\ &= \int_{e_l} \epsilon(\boldsymbol{x}) \boldsymbol{E}(\boldsymbol{x}) \cdot \mathrm{d}\boldsymbol{S} && (2.25)\\ &= -\int_{e_l} \epsilon(\boldsymbol{x}) \nabla u(\boldsymbol{x}) \cdot \mathrm{d}\boldsymbol{S} && (2.26)\\ &= -\int_{e_l} \epsilon(\boldsymbol{x}) \nabla u(\boldsymbol{x}) \cdot \boldsymbol{\nu} \mathrm{d}S && (2.27)\\ &= -\int_{e_l} \epsilon(\boldsymbol{x}) \frac{\partial u(\boldsymbol{x})}{\partial \boldsymbol{\nu}} \mathrm{d}S. && (2.28) \end{aligned}$$

In practice, the Poisson equation (2.17) is often solved numerically, for example, with the help of the finite element method (FEM), for example. In that case, the permittivity distribution can be discretized as

$$\epsilon(\boldsymbol{x}) = \sum_{i=1}^{n} \epsilon_i \phi_i(\boldsymbol{x}), \tag{2.29}$$

where $\phi_i(\boldsymbol{x})$ are the chosen basis functions for the permittivity distribution and n is the number of discretization points. Moreover, it is denoted that $\boldsymbol{\epsilon} = [\epsilon_1, \epsilon_2, \cdots, \epsilon_n]^{\mathrm{T}}$ is the vector representation of

$\epsilon(\boldsymbol{x})$. The potentials are now solved from the discretized form of equation (2.17), and the potential distribution after the discretatization is of the form

$$u(\boldsymbol{x}) \approx u_h(\boldsymbol{x}) = \sum_{i=1}^{N} u_i \varphi_i(\boldsymbol{x}), \tag{2.30}$$

where $\varphi_i(\boldsymbol{x})$ are the chosen basis functions for the potential distribution and N is the number of discretization points. The vector representation for $u_h(\boldsymbol{x})$ is $\boldsymbol{u} = [u_1, u_2, \cdots, u_N]^{\mathrm{T}}$.

The observation model for ECT measurements can be written using the equation (2.28), and it is of the form

$$\boldsymbol{Q} = \boldsymbol{q}(\boldsymbol{\epsilon}) + \boldsymbol{v}_q \,, \tag{2.31}$$

where $\boldsymbol{Q} = [Q_1, Q_2, \cdots, Q_m]^{\mathrm{T}}$ is a vector containing the measured electric charges, m is the number of measurements, $\boldsymbol{q} = [q_1(\boldsymbol{\epsilon}), q_2(\boldsymbol{\epsilon}), \cdots, q_m(\boldsymbol{\epsilon})]^{\mathrm{T}}$ connects the permittivity distribution with the electric charges, and $\boldsymbol{v}_q = [v_1^q, v_2^q, \cdots, v_m^q]^{\mathrm{T}}$ is the additive measurement noise.

For numerical implementations, the variational form and the FEM-approximation of the 3D-ECT forward problem is presented in the Appendix. Other descriptions of the numerical implementation can be found in [79, 80].

2.1.2 Inverse problem

In the inverse problem, the permittivity distribution is solved with the help of the known electric charge data $\boldsymbol{Q}$. A common method in electrical tomography is to use *difference imaging* [81]. In the difference reconstuction method, the permittivity distribution is estimated based on the differences between the measured and the reference data.

In the derivation of the method, linearization of the model (2.28) is needed: the Taylor series expansion at a chosen linearization

point $\boldsymbol{\epsilon}_{\text{lin}}$ is of the form

$$\begin{aligned} q_l(\boldsymbol{\epsilon}) =& q_l(\boldsymbol{\epsilon}_{\text{lin}}) + \sum_{i=1}^{n} \frac{\partial q_l}{\partial \epsilon_i}(\epsilon_i - \epsilon_i^{\text{lin}}) \\ &+ \frac{1}{2!} \sum_{i=1}^{n} \sum_{j=1}^{n} \frac{\partial^2 q_l}{\partial \epsilon_i \partial \epsilon_j}(\epsilon_i - \epsilon_i^{\text{lin}})(\epsilon_j - \epsilon_j^{\text{lin}}) + \cdots \end{aligned} \tag{2.32}$$

Next, the Taylor series is approximated by omitting the higher order derivatives

$$q_l(\boldsymbol{\epsilon}) \approx q_l(\boldsymbol{\epsilon}_{\text{lin}}) + \sum_{i=1}^{n} \frac{\partial q_l}{\partial \epsilon_i}(\epsilon_i - \epsilon_i^{\text{lin}}). \tag{2.33}$$

When the same approximation is used for all the electric charges, the following matrix equation is formed

$$\boldsymbol{q}(\boldsymbol{\epsilon}) \approx \boldsymbol{q}(\boldsymbol{\epsilon}_{\text{lin}}) + \boldsymbol{J}_{\boldsymbol{\epsilon}_{\text{lin}}}(\boldsymbol{\epsilon} - \boldsymbol{\epsilon}_{\text{lin}}). \tag{2.34}$$

Here, $\boldsymbol{J}_{\boldsymbol{\epsilon}_{\text{lin}}} = \boldsymbol{J}$ is the Jacobian matrix (sometimes referred to as the sensitivity matrix) computed at the linearization point. The Jacobian is an $m \times n$ matrix and it is defined as

$$\boldsymbol{J} = \begin{bmatrix} \frac{\partial q_1}{\partial \epsilon_1} & \frac{\partial q_1}{\partial \epsilon_2} & \cdots & \frac{\partial q_1}{\partial \epsilon_n} \\ \frac{\partial q_2}{\partial \epsilon_1} & \frac{\partial q_2}{\partial \epsilon_2} & \cdots & \frac{\partial q_2}{\partial \epsilon_n} \\ \vdots & & \ddots & \vdots \\ \frac{\partial q_m}{\partial \epsilon_1} & \frac{\partial q_m}{\partial \epsilon_2} & \cdots & \frac{\partial q_m}{\partial \epsilon_n} \end{bmatrix}. \tag{2.35}$$

Next, the approximation of the observation model for measured charges $\boldsymbol{Q}$ and for reference charges $\boldsymbol{Q}_{\text{ref}} = \left[Q_1^{\text{ref}}, \ldots, Q_m^{\text{ref}}\right]^{\text{T}}$ can be written as

$$\boldsymbol{Q} \approx \boldsymbol{q}(\boldsymbol{\epsilon}_{\text{lin}}) + \boldsymbol{J}(\boldsymbol{\epsilon} - \boldsymbol{\epsilon}_{\text{lin}}) + \boldsymbol{v}_q \tag{2.36}$$

$$\boldsymbol{Q}_{\text{ref}} \approx \boldsymbol{q}(\boldsymbol{\epsilon}_{\text{lin}}) + \boldsymbol{J}(\boldsymbol{\epsilon}_{\text{ref}} - \boldsymbol{\epsilon}_{\text{lin}}) + \boldsymbol{v}_{q,\text{ref}}. \tag{2.37}$$

The linearized permittivity distribution $\boldsymbol{\epsilon}_{\text{lin}}$ is often the same as the reference distribution $\boldsymbol{\epsilon}_{\text{ref}}$. Next, the equations (2.36) and (2.37) are subtracted

$$\boldsymbol{Q} - \boldsymbol{Q}_{\text{ref}} \approx \boldsymbol{J}(\boldsymbol{\epsilon} - \boldsymbol{\epsilon}_{\text{ref}}) + \delta \boldsymbol{v}_q, \tag{2.38}$$

where $\delta \boldsymbol{v}_q = \left[(\boldsymbol{v}_1^q - \boldsymbol{v}_1^{q,\mathrm{ref}}), \ldots, (\boldsymbol{v}_m^q - \boldsymbol{v}_m^{q,\mathrm{ref}})\right]^{\mathrm{T}}$ is the difference of the noise terms. The permittivity distribution which is to be solved is the solution of the following minimization problem

$$\min_{\boldsymbol{\epsilon}} \left\{ \left\| (\boldsymbol{Q} - \boldsymbol{Q}_{\mathrm{ref}}) - \boldsymbol{J}(\boldsymbol{\epsilon} - \boldsymbol{\epsilon}_{\mathrm{ref}}) \right\|^2 \right\}, \tag{2.39}$$

where the norm is the 2-norm in $\mathbb{R}^n$. The minimization problem, however, is ill-posed, and usually it is replaced with a well-posed problem that is achieved with the help of regularization. In this case, the well-posed problem that utilizes Tikhonov regularization is

$$\min_{\boldsymbol{\epsilon}} \left\{ \left\| (\boldsymbol{Q} - \boldsymbol{Q}_{\mathrm{ref}}) - \boldsymbol{J}(\boldsymbol{\epsilon} - \boldsymbol{\epsilon}_{\mathrm{ref}}) \right\|^2 + \alpha \left\| \boldsymbol{L}(\boldsymbol{\epsilon} - \boldsymbol{\epsilon}_{\mathrm{ref}}) \right\|^2 \right\}. \tag{2.40}$$

Here, the regularization term is $\alpha \left\| \boldsymbol{L}(\boldsymbol{\epsilon} - \boldsymbol{\epsilon}_{\mathrm{ref}}) \right\|^2$, where α is a positive scalar and called the regularization parameter, and $\boldsymbol{L}$ is called the regularization matrix. The solution of this minimization problem is

$$\begin{aligned} & \boldsymbol{\epsilon} - \boldsymbol{\epsilon}_{\mathrm{ref}} &&= (\boldsymbol{J}^{\mathrm{T}}\boldsymbol{J} + \alpha \boldsymbol{L}^{\mathrm{T}}\boldsymbol{L})^{-1} \boldsymbol{J}^{\mathrm{T}} (\boldsymbol{Q} - \boldsymbol{Q}_{\mathrm{ref}}) && (2.41) \\ \Leftrightarrow \quad & \boldsymbol{\epsilon} - \boldsymbol{\epsilon}_{\mathrm{ref}} &&= \boldsymbol{K}(\boldsymbol{Q} - \boldsymbol{Q}_{\mathrm{ref}}). && (2.42) \end{aligned}$$

One benefit of this method is that the difference of the measurement data can cancel out some static measurement errors. Furthermore, the method is fast to compute since the computations consist of only one matrix-vector multiplication. This is because the matrix $\boldsymbol{K}$ can be computed beforehand.

The drawback of the difference reconstruction method is that it is not always possible to measure the reference data, and sometimes further accuracy is required. In those cases, *absolute imaging* techniques can be used. As an example, the minimization problem

$$\min_{\boldsymbol{\epsilon}} \left\{ \left\| (\boldsymbol{Q} - \boldsymbol{q}(\boldsymbol{\epsilon})) \right\|^2 + \alpha \left\| \boldsymbol{L}(\boldsymbol{\epsilon} - \boldsymbol{\epsilon}_{\mathrm{pr}}) \right\|^2 \right\} \tag{2.43}$$

can be solved with the help of the iterative Gauss-Newton method: the ith iteration is of the form

$$\boldsymbol{\epsilon}_{i+1} = \boldsymbol{\epsilon}_i + \kappa_i (\boldsymbol{J}_i^{\mathrm{T}}\boldsymbol{J}_i + \alpha \boldsymbol{L}^{\mathrm{T}}\boldsymbol{L})^{-1} \left[(\boldsymbol{J}_i^{\mathrm{T}} (\boldsymbol{Q} - \boldsymbol{q}(\boldsymbol{\epsilon}_i)) - \alpha \boldsymbol{L}^{\mathrm{T}}\boldsymbol{L}(\boldsymbol{\epsilon}_i - \boldsymbol{\epsilon}_{\mathrm{pr}}) \right], \tag{2.44}$$

where κ_i is the step parameter, $\boldsymbol{q}(\boldsymbol{\epsilon}_i)$ contains the electric charges computed from the forward model with $\boldsymbol{\epsilon}_i$, and $\boldsymbol{\epsilon}_{\mathrm{pr}}$ is the prior assumption of the permittivity distribution. Usually, the iterative Gauss-Newton gives better estimates of the desired distributions. However, the estimates are slower to compute, and the method can fail if the measured data contains static errors or the forward model is inaccurate.

It is worth noting, that the permittivity distribution is not always the quantity of interest in ECT. Sometimes it is more important to obtain information about the concentration, moisture or density distribution, for example. This can be done through composite mapping. The requirement is that the mapping between the quantity of interest and the permittivity has to be defined.

2.2 ELECTRICAL IMPEDANCE TOMOGRAPHY

2.2.1 Forward problem

In contrast to ECT, in EIT the studied medium can contain both electrically conductive and dielectric properties. The imaging domain Ω in EIT is depicted in figure 2.2. It consists of the region of interest and the electrodes; external shielding is not always necessary.

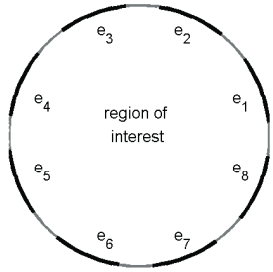

Figure 2.2: A typical EIT sensor consists of the region of interest and the electrodes. The boundaries between the electrodes are insulating.

Here, it is assumed that the excitation signals are time-harmonic electric currents and therefore the time-harmonic Maxwell equa-

tions are used

$$\nabla \times \boldsymbol{E}(\boldsymbol{x}) = -\mathrm{i}\omega \boldsymbol{B}(\boldsymbol{x}) \,, \tag{2.45}$$

$$\nabla \times \boldsymbol{H}(\boldsymbol{x}) = \boldsymbol{j}(\boldsymbol{x}) + \mathrm{i}\omega \boldsymbol{D}(\boldsymbol{x}) \,, \tag{2.46}$$

$$\nabla \cdot \boldsymbol{D}(\boldsymbol{x}) = \rho(\boldsymbol{x}) \,, \tag{2.47}$$

$$\nabla \cdot \boldsymbol{B}(\boldsymbol{x}) = 0 \,, \tag{2.48}$$

where ω is the angular frequency and i is the imaginary unit. Next, the quasi-static approximation is made: the term $-\mathrm{i}\omega \boldsymbol{B}(\boldsymbol{x})$ in equation (2.45) is assumed to be negligible which is valid with the frequencies that are usually used in EIT. This leads to the equation

$$\nabla \times \boldsymbol{E}(\boldsymbol{x}) = 0. \tag{2.49}$$

As in ECT, this implies that

$$\boldsymbol{E}(\boldsymbol{x}) = -\nabla u(\boldsymbol{x}). \tag{2.50}$$

Next, the equations (2.5) and (2.7) are inserted in (2.46)

$$\nabla \times \boldsymbol{H}(\boldsymbol{x}) = \sigma \boldsymbol{E}(\boldsymbol{x}) + \mathrm{i}\omega\epsilon \boldsymbol{E}(\boldsymbol{x}). \tag{2.51}$$

Taking the divergence on both sides of (2.51) and using the fact that $\nabla \cdot \nabla \times \boldsymbol{H}(\boldsymbol{x}) = 0$ gives the equation

$$\nabla \cdot \nabla \times \boldsymbol{H}(\boldsymbol{x}) = \nabla \cdot (\sigma + \mathrm{i}\omega\epsilon)\boldsymbol{E}(\boldsymbol{x}) \tag{2.52}$$

$$\Leftrightarrow \quad \nabla \cdot (\sigma + \mathrm{i}\omega\epsilon)\nabla u(\boldsymbol{x}) = 0. \tag{2.53}$$

For the rest of the section it will be assumed that the capacitive effects are negligible[2,3] ($\sigma \gg \omega\epsilon$) which results in

$$\nabla \cdot \sigma \nabla u(\boldsymbol{x}) = 0. \tag{2.54}$$

[2]Strictly speaking, this is the assumption that is made in electrical resistance tomography (ERT).

[3]For time-harmonic ECT excitation signals, it is assumed that $\omega\epsilon \gg \sigma$ which also results in equation (2.17) after the imaginary unit and the angular frequency are omitted.

A condition for the boundary current density can be formulated with the help of (2.7) and (2.50). The normal component of the current density is

$$\boldsymbol{j}_\eta(\boldsymbol{x}) = -\sigma(\boldsymbol{x})\boldsymbol{E}_\eta(\boldsymbol{x}) \tag{2.55}$$

$$= \sigma(\boldsymbol{x})\nabla u(\boldsymbol{x}) \cdot \boldsymbol{\eta} \tag{2.56}$$

$$= \sigma(\boldsymbol{x})\frac{\partial u(\boldsymbol{x})}{\partial \boldsymbol{\eta}}, \tag{2.57}$$

where $\boldsymbol{\eta}$ is the outward unit normal vector[4]. Now, by integrating this over the surface of the electrode one obtains

$$I_{e_l} = \int_{e_l} \sigma(\boldsymbol{x})\frac{\partial u(\boldsymbol{x})}{\partial \boldsymbol{\eta}}\mathrm{d}S, \tag{2.58}$$

where e_l is the surface of the lth electrode and I_{e_l} is the electric current through the lth electrode. The electric current through other boundaries is zero which is mathematically presented as

$$\sigma(\boldsymbol{x})\frac{\partial u(\boldsymbol{x})}{\partial \boldsymbol{\eta}} = 0. \tag{2.59}$$

Furthermore, a boundary condition for measured voltages is formulated as

$$U_l(\sigma) = u(\boldsymbol{x}) + z_l\sigma(\boldsymbol{x})\frac{\partial u(\boldsymbol{x})}{\partial \boldsymbol{\eta}}, \tag{2.60}$$

where z_l and U_l are the contact impedance and the voltage related to the lth electrode. The contact impedances are used to model the potential drop that occurs when the electric current penetrates the studied medium from the surface of the electrode. Often the charge carriers of electric current change from electrons to ions at the boundary. This model is called *the complete electrode model* [82, 83].

Because the Kirchoff's laws for electric current and voltage also

[4]Here the word "outward" means outwards from the domain boundary.

apply here, it is required that

$$\sum_{l=1}^{N_e} I_l = 0, \tag{2.61}$$

$$\sum_{l=1}^{N_e} U_l = 0. \tag{2.62}$$

The electric potential distribution and the voltages at the electrodes are usually solved numerically. For that, the conductivity and the potential distribution need to be discretized. If the discretization is carried out similarly as in ECT, then $\sigma(\boldsymbol{x})$ can be presented as $\boldsymbol{\sigma} = [\sigma_1, \sigma_2, \cdots, \sigma_n]^{\mathrm{T}}$ and $u(\boldsymbol{x})$ as $\boldsymbol{u} = [u_1, u_2, \cdots, u_N]^{\mathrm{T}}$.

The observation model for EIT measurements can be written with the help of the discretized form of equation (2.60) so that it is of the form

$$\boldsymbol{V} = \boldsymbol{U}(\sigma) + \boldsymbol{v}_v, \tag{2.63}$$

where $\boldsymbol{V} = [V_1, V_2, \cdots, V_m]^{\mathrm{T}}$ is a vector containing the measured voltages, m is the number of measurements, $\boldsymbol{U} = [U_1(\sigma), U_2(\sigma), \cdots, U_m(\sigma)]^{\mathrm{T}}$ connects the conductivity distribution with the measured voltages, and $\boldsymbol{v}_v = [v_1^v, v_2^v, \cdots, v_m^v]^{\mathrm{T}}$ is the additive measurement noise.

In the complete electrode model it is possible to consider also the contact impedances as variables. In that case, the observation model is of the form

$$\boldsymbol{V} = \boldsymbol{U}(\sigma, \boldsymbol{z}) + \boldsymbol{v}_v, \tag{2.64}$$

where $\boldsymbol{U} = [U_1(\sigma, \boldsymbol{z}), U_2(\sigma, \boldsymbol{z}), \cdots, U_m(\sigma, \boldsymbol{z})]^{\mathrm{T}}$ and $\boldsymbol{z} = [z_1, z_2, \cdots, z_{N_e}]^{\mathrm{T}}$ contains the contact impedances of the electrodes, and N_e is the number of electrodes.

For numerical implementations, the variational form and the FEM-approximation for the complete electrode model have been presented in [81, 82]. Other electrode models can be found in [83].

2.2.2 Inverse problem

In the EIT inverse problem, the electric conductivity distribution is solved with the help of the known currents and voltages. The difference reconstruction formula for EIT can be derived similarly as in ECT, and the result is of the form

$$\sigma - \sigma_{\text{ref}} = (\boldsymbol{J}^{\text{T}}\boldsymbol{J} + \alpha \boldsymbol{L}^{\text{T}}\boldsymbol{L})^{-1}\boldsymbol{J}^{\text{T}}(\boldsymbol{V} - \boldsymbol{V}_{\text{ref}}) \tag{2.65}$$

$$\Leftrightarrow \quad \sigma - \sigma_{\text{ref}} = \boldsymbol{K}(\boldsymbol{V} - \boldsymbol{V}_{\text{ref}}), \tag{2.66}$$

where $\boldsymbol{V}_{\text{ref}}$ is a vector containing the measured reference voltages and $\boldsymbol{J}$ is the Jacobian matrix which is of the form

$$\boldsymbol{J} = \begin{bmatrix} \frac{\partial U_1}{\partial \sigma_1} & \frac{\partial U_1}{\partial \sigma_2} & \cdots & \frac{\partial U_1}{\partial \sigma_n} \\ \frac{\partial U_2}{\partial \sigma_1} & \frac{\partial U_2}{\partial \sigma_2} & \cdots & \frac{\partial U_2}{\partial \sigma_n} \\ \vdots & & \ddots & \vdots \\ \frac{\partial U_m}{\partial \sigma_1} & \frac{\partial U_m}{\partial \sigma_2} & \cdots & \frac{\partial U_m}{\partial \sigma_n} \end{bmatrix}. \tag{2.67}$$

For absolute imaging, the corresponding ith iteration of the Gauss-Newton method is of the form

$$\sigma_{i+1} = \sigma_i + \kappa_i(\boldsymbol{J}_i^{\text{T}}\boldsymbol{J}_i + \alpha \boldsymbol{L}^{\text{T}}\boldsymbol{L})^{-1}\left[(\boldsymbol{J}_i^{\text{T}}(\boldsymbol{V} - \boldsymbol{U}(\sigma_i)) - \alpha \boldsymbol{L}^{\text{T}}\boldsymbol{L}(\sigma_i - \sigma_{\text{pr}})\right], \tag{2.68}$$

where σ_{pr} is the prior assumption of the conductivity distribution.

If the contact impedances are considered as unknowns, they can be estimated along with the conductivity distribution in the inverse problem [84,85]. In that case, the difference reconstruction formula can be presented as

$$\begin{bmatrix} \sigma \\ z \end{bmatrix} - \begin{bmatrix} \sigma_{\text{ref}} \\ z_{\text{ref}} \end{bmatrix} = (\widetilde{\boldsymbol{J}}^{\text{T}}\widetilde{\boldsymbol{J}} + \widetilde{\boldsymbol{L}}^{\text{T}}\widetilde{\boldsymbol{L}})^{-1}\widetilde{\boldsymbol{J}}^{\text{T}}(\boldsymbol{V} - \boldsymbol{V}_{\text{ref}}) \tag{2.69}$$

$$\Leftrightarrow \quad \widetilde{\sigma} - \widetilde{\sigma}_{\text{ref}} = \widetilde{\boldsymbol{K}}(\boldsymbol{V} - \boldsymbol{V}_{\text{ref}}). \tag{2.70}$$

If the conductivity distribution is assumed to be independent of the contact impedances, the Jacobian, the regularization parameters

and the regularization matrices are of the form

$$\widetilde{\boldsymbol{J}} = [\boldsymbol{J} \quad \boldsymbol{J}_z], \tag{2.71}$$

$$\widetilde{\boldsymbol{L}} = \begin{bmatrix} \sqrt{\alpha}\boldsymbol{L} & 0 \\ 0 & \sqrt{\alpha_z}\boldsymbol{L}_z \end{bmatrix}, \tag{2.72}$$

where $\boldsymbol{J}$ is the same as in (2.67), and α_z and $\boldsymbol{L}_z$ are the regularization parameter and the matrix for contact impedances. The Jacobian matrix for contact impedances is of the form

$$\boldsymbol{J}_z = \begin{bmatrix} \frac{\partial U_1}{\partial z_1} & \frac{\partial U_1}{\partial z_2} & \cdots & \frac{\partial U_1}{\partial z_{N_e}} \\ \frac{\partial U_2}{\partial z_1} & \frac{\partial U_2}{\partial z_2} & \cdots & \frac{\partial U_2}{\partial z_{N_e}} \\ \vdots & & \ddots & \vdots \\ \frac{\partial U_m}{\partial z_1} & \frac{\partial U_m}{\partial z_2} & \cdots & \frac{\partial U_m}{\partial z_{N_e}} \end{bmatrix}. \tag{2.73}$$

The corresponding ith iteration of the Gauss-Newton method in this case is of the form

$$\widetilde{\sigma}_{i+1} = \widetilde{\sigma}_i + \kappa_i(\widetilde{\boldsymbol{J}}_i^{\mathrm{T}}\widetilde{\boldsymbol{J}}_i + \widetilde{\boldsymbol{L}}^{\mathrm{T}}\widetilde{\boldsymbol{L}})^{-1}\left[(\widetilde{\boldsymbol{J}}_i^{\mathrm{T}}(\boldsymbol{V} - \boldsymbol{U}(\widetilde{\sigma}_i)) - \widetilde{\boldsymbol{L}}^{\mathrm{T}}\widetilde{\boldsymbol{L}}(\widetilde{\sigma}_i - \widetilde{\sigma}_{\mathrm{pr}})\right], \tag{2.74}$$

where $\widetilde{\sigma}_{\mathrm{pr}}$ contains the prior assumptions for the conductivity distribution and contact impedances.

The simultaneous estimation of contact impedance values in a dynamic process can be advantageous if the contact impedance values are expected to change during the process, for example, due to contamination.

2.3 RECONSTRUCTION METHODS IN ELECTRICAL TOMOGRAPHY

In the *deterministic framework*, there are numerous methods available to solve the imaging problems; some of them are described and compared in [71,76,80,86–88]. In some cases, it can be beneficial to formulate the imaging problem as a non-stationary state-estimation

problem and to use a suitable Kalman filter -type approach[5] [89–95]. Another approach is to consider the imaging problem as an inverse scattering problem and, for example, to utilize the D-bar method [96–98].

The inverse problems can also be formulated using the *Bayesian framework* in which all the model variables are considered as random variables with probability distributions [99, 100]. More information about this in electrical tomography can be found in [73, 99–102]. Recently the approximation error theory was developed within the Bayesian framework [99]. In electrical tomography, it enables for example the reduction and simplification of the forward model without any significant loss in accuracy [103–106].

2.4 MEASUREMENT SYSTEMS

Electrical tomography systems consist of measurement electronics, sensors and software. The systems are often engineered inhouse. However, there are also a few commercial companies such as Process Tomography Ltd.[6], Industrial Tomography Systems Plc.[7] and Numcore Oy[8] that provide these systems.

The electronics can be encased in a separate measurement unit or integrated inside a sensor. The benefit of separate measurement units is that they are moveable and they can be used for various targets, but then again a suitable sensor needs to be appropriately designed and customized for each application. The benefit of sensors with integrated measurement electronics is that they are not so prone to electrical noise caused by the surroundings. Especially in ECT, integrated electronics can be useful since it eliminates the need of long measurement wires that can cause significant stray capacitances [107]. The obvious drawback is that these sensors often

[5]The methods that are based on Kalman filters can be considered statistical because of their primary assumptions, even though deterministic algorithms are often used in solving the inverse problems.

[6]http://www.tomography.com/

[7]http://www.itoms.com/

[8]http://www.numcore.com/

are not suitable for other targets. Generally speaking, for laboratory scale studies and for multiple targets a separate measurement unit may be a better choice, and a sensor with integrated electronics may be better for industrial surroundings and for permanent targets.

In a common measurement pattern, one of the electrodes is first excited and the rest are used for measurements. After that the excitation electrode is changed and the measurements are carried out with the rest, and this is repeated until there is enough measurement data. In ECT, the excitation can be carried out with a potential signal and in EIT with an alternating electric current. The excitation and measurement patterns have an effect on the resolution; however, these patterns might not be adjustable in commercial measurement units. For ERT/EIT, different excitation and measurement patterns have been studied for example in [108–111].

More information on ECT and ERT/EIT measurement electronics can be found from [107, 112–117] and [118–124], respectively. More information on ECT sensors can be found from [54, 125–127]. For ERT/EIT, there is less literature specifically on designing sensors; this may be due to the fact that the data acquisition is not as sensitive as in ECT[9]. A few different electrode types were presented in [43], and some general guidelines to design ERT/EIT sensors were described in [63]. Moreover, an ERT/EIT sensor with electrically conducting walls was analyzed in [128].

Depending on the target, one can choose either 2D or 3D tomography; however, 3D-ECT is not yet commercially available due to the limited availability of 3D-ECT algorithms. In general, 2D-tomography can be used in cases where only a cross-section of the target is needed, and 3D-tomography when one needs to determine variations inside the target in all spatial directions. Usually, the use of 3D-tomography improves the quality of the image, even in those

[9]One reason for this could be that excitation in ECT is often carried out with a fixed excitation potential (as in this study) and thus the only way to adjust the value of the measured charge (capacitance) is to either change the diameter of the sensor or the size of the electrodes. However in EIT, the excitation is often carried out with electric currents that can be adjusted according to the need.

cases where only a 2D cross-section of the whole image would ultimately be needed; this is due to the fact that the electric fields that are used for measurements are always three-dimensional in nature. In some cases, linear sensors can provide all the necessary information, for example when one only needs to estimate the depth profile of the target [44,45,47,129,130].

The manufacturers usually provide the user with a reconstruction software. The software can be applicable only for simple geometries and for fixed measurement protocols. Therefore, inhouse reconstruction codes are in many cases strongly recommended, since often significant customization based on each target is required. There are also free software packages available such as the Electrical impedance tomography and diffuse optical tomography reconstruction software (EIDORS) package[10,11] to get started [131,132].

[10] http://venda.uku.fi/~mvauhkon/MatlabEIT2d.html
[11] http://eidors3d.sourceforge.net/

3 Review on studies

3.1 STUDY 1: HIGH-SHEAR GRANULATION OF PHARMACEUTICAL POWDERS

This section reviews the work that was presented in Publication **I**. In this study, high-shear granulation processes were monitored with 2D electrical capacitance tomography, and the processes were evaluated and characterized with the help of ECT tomograms and mixing index curves.

3.1.1 Methods

For the study, an ECT sensor was engineered and it consisted of a plastic vessel, six electrodes with inter-electrode screens patterned on two printed circuit boards (PCBs), an external brass screen and a removable lid (see figure 3.1(b)-(d)). The size and the amount of the electrodes were chosen to compromise the diameter of the vessel, the signal-to-noise ratio and the measurement range of the ECT system. PTL300E (Process Tomography Ltd.) electrical capacitance tomography system was utilized to measure absolute values of capacitances.

A vertical high-shear mixer (Donsmark QMM-1 Micro Mixer) equipped with a plastic three-blade impeller was used for mixing in the experiments (see figure 3.1(a) and (c)). A peristaltic pump and a nozzle were used for liquid addition (see figure 3.1(d)).

An inhouse image reconstruction algoritm that utilized the difference reconstruction method explained in section 2.1.2 was used to estimate the relative permittivity distribution inside the sensor. The algorithm was customized to take into account the mixer shaft that stuck out from the center of the sensor during the experiments. The shaft was made of metal and kept electrically grounded. First, the electric potential distribution was solved by setting the surfaces of the shaft to zero potential, and then by computing the corre-

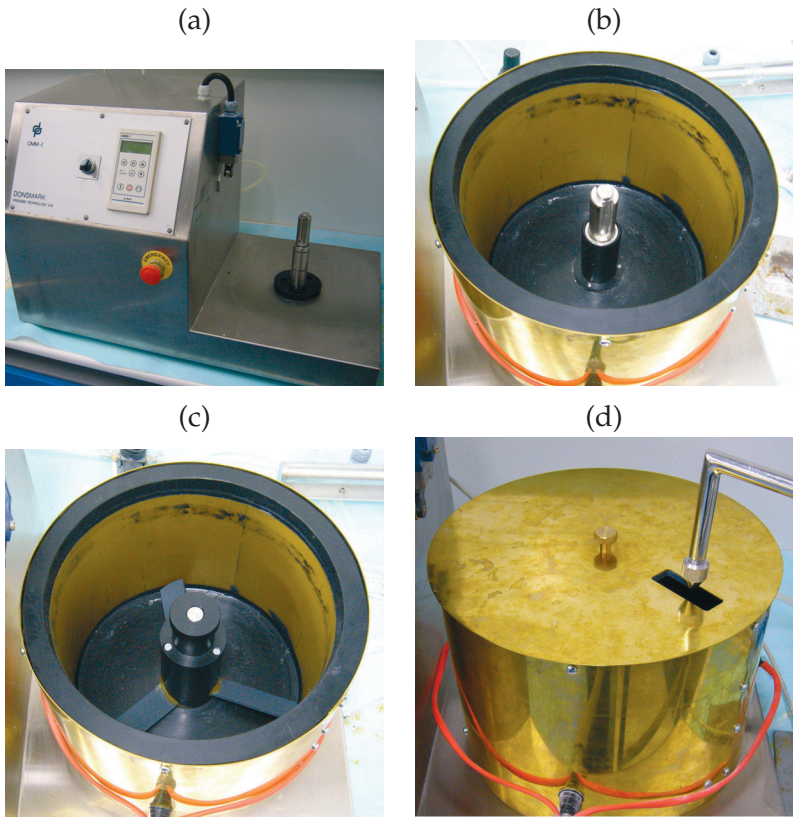

Figure 3.1: (a): The high-shear mixer that was used in the experiments. (b): The ECT sensor is placed on the mixer, and the mixer shaft sticks out from centre of the sensor. (c): The ECT sensor and the three-bladed impeller that was made of plastic. (d): During the granulation experiments, the liquid was added with the help of a peristaltic pump and a nozzle through a hole in the sensor lid.

sponding sensitivity distributions. Figure 3.2 shows the sensitivity distribution inside the sensor when the capacitance is measured from opposite electrodes in the case of the traditional circular sensor and in the case when the shaft is in the centre. As can be seen, the sensitivity is significantly different when the shaft is present. This clearly emphasizes why the standard techniques developed for circular objects do not produce satisfactory tomograms with this kind of geometry [133].

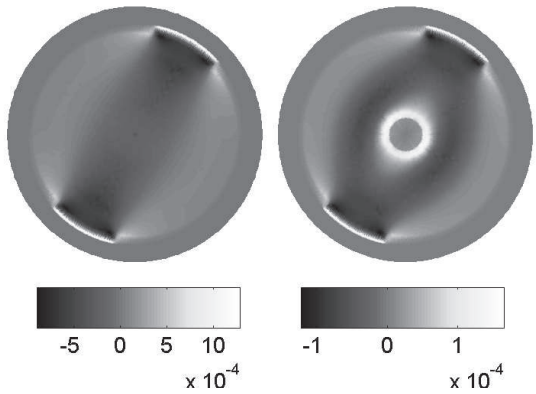

Figure 3.2: Left: The sensitivity inside the sensor corresponding to opposite capacitance measurement in a traditional circular case. Right: The sensitivity is clearly different when there is a grounded boundary in the centre (this situation corresponds to figure 3.1(b)).

3.1.2 Materials and experiments

Four granulations were monitored with ECT. All the independent mutual capacitances were measured 300 times per second. In each experiment, the mass of the microcrystalline cellulose (MCC) powder was 500 g, the binder liquid was 5% w/w polyvinylpyrrolidone (PVP) (Povidone K-25 grade BASF Se) in water solution and the liquid addition rate was 42 ml/min. A constant impeller rotation speed was used in each experiment: 150, 250, 350 and 450 rpm. The duration of each experiment was 14 min 45s: the first 45 s simulated the powder mixing process, liquid was added for the next 12 min and the last 2 min was used for wet massing.

3.1.3 Results and Discussion

Figure 3.3 shows tomograms that represent the granulation processes at various time instants. It can be seen that in the final state there are higher relative permittivity values in the 150 rpm granulation (figures 3.3 (m)) whereas there are lower permittivity values in the higher impeller speed granulations (figures 3.3 (n)-(p)) even though the same amount of powder and liquid was used in every experiment. The differences are due to different horizontal and vertical mixing properties related to the impeller rotation speed. Firstly, the added liquid remained mostly at the bottom of the sensor (the most sensitive region) if the impeller speed was too low, but it was distributed more homogenously in the vertical direction (to the less sensitive regions) if the impeller speed was high. Secondly, a higher impeller speed spread the wet powder bed to a wider area in the vertical direction. Thirdly, if the shear was too low to form compact granules, then the powder and the liquid clumped at the bottom and caused high permittivity values, whereas if the shear was high enough to form compact granules, then the granules took up more space (air) around each other which resulted effectively as lower permittivity values.

Based on the sieving analysis and the visual observations of the end products, the granulations corresponding to 150 and 250 rpm could be classified as unsuccessful whereas 350 rpm and 450 rpm granulations were successful. The evaluation criteria used were the homogeneity of the granule size and whether the granules could hold together or not. Large agglomerates were observed in the unsuccessful granulations. Based on this and the previous analysis that high permittivities were reconstructed if the mixing speed was slow, the ECT tomograms could be used as indicators of whether the mixer speed had been sufficient to achieve a successful granulation. This was evident especially at the lowest mixer speed which produced the worst outcome and clearly the highest reconstructed permittivity values at the end.

Figure 3.4 shows the behaviour of the mixer power consump-

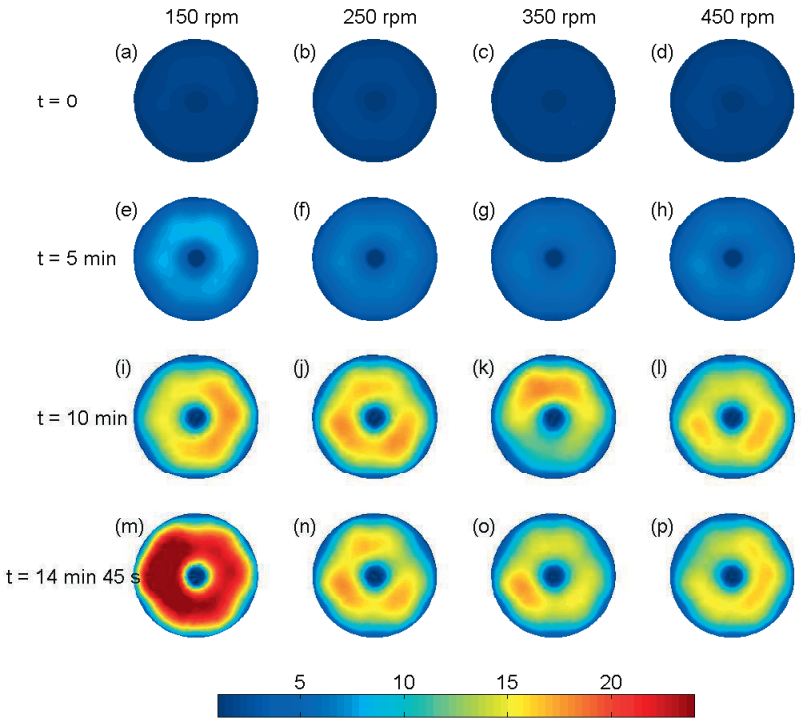

Figure 3.3: The relative permittivity distributions at the beginning (a)-(d), after five minutes (e)-(h), after ten minutes (i)-(l) and at the end (m)-(p) of the granulation experiments.

tion during the 450 rpm granulation and the mixing index curve that was calculated from the tomograms. The mixing index (or the relative standard deviation) is defined as the ratio of the standard deviation of the reconstructed permittivities and the mean value of the permittivities. The dashed vertical lines in figure 3.4 represent the time points when the liquid addition was first turned on and then subsequently stopped.

The power consumption curve was analyzed according to previous reports [20, 134]. Based on the analysis, between $t = 45$ s (when the liquid addition was turned on) and $t = 3$ min 45 s (the first solid vertical line), granulation liquid is absorbed by the powder but liquid bridges have not yet formed. At these time points, the power consumption does not increase. The liquid bridges begin to form at $t = 3$ min 45 s, which can be seen as a rapid increase in the power consumption curve. This pendular state lasts until $t = 8$ min (the second solid vertical line), after which a plateau phase is reached. This is a transition state between the pendular and the funicular states. The funicular state begins at $t = 11$ min (the third solid vertical line) and ends when the liquid addition is stopped at $t = 12$ min 45 s.

It can be seen that at the same time points there are also changes in the mixing index and its derivative which indicates that the phases of the process and the states of the granules could be determined based on these curves as well. During the liquid uptake, the mixing index increases rapidly. At the beginning of the pendular state, there is an abrupt change in the slope which can also be seen as a decline in the mixing index derivative. The beginning of the transition state evokes also a small change in the mixing index curve. Finally, at the beginning of the funicular state, the mixing index curve levels off which can also be seen as derivative values approaching zero.

Figure 3.5 presents the mixing index curves and their derivatives as a function of time during the granulations. As can be seen, the slope changes that were explained earlier are clearly visible in all the experiments. During the successful processes (that is the 350

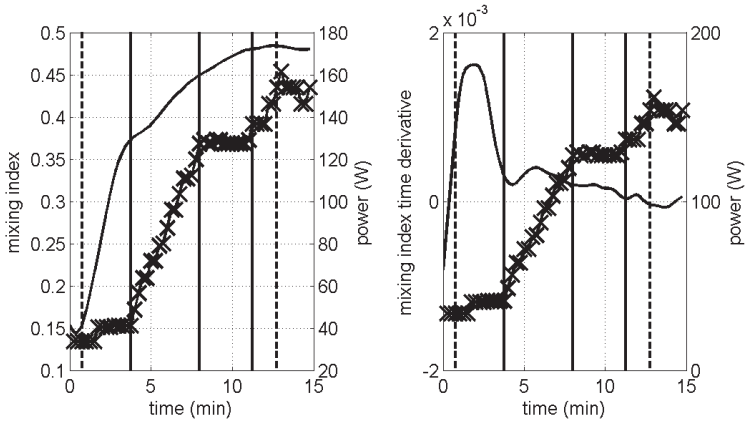

Figure 3.4: The mixing index and its time derivative (solid lines) from the 450 rpm granulation with the corresponding power consumption curve (solid line with crosses). It can be seen, that at the same time points when there are changes in the power consumption curve there are also changes in the mixing index curve.

rpm and 450 rpm processes) the mixing index levels off at the end which can also be seen as derivative values close to zero; the derivative at the end of the unsuccessful 150 rpm process does not level off towards zero. From the monitoring point of view, the levelling off could be used as an indicator of the time when to stop liquid addition (and to begin the wet massing) or even as an end-point criterion in the process if the formulation and end-product quality criteria have been achieved. Moreover, the pendular state begins later in the 150 rpm process than in the other processes.

The 250 rpm granulation could not be considered as a fully successful granulation based on the visual and sieve analysis of the final product even though the levelling off of the mixing index was observed. Apparently, the difference between the 250 rpm and the successful granulations was not clear enough for the ECT technique to detect.

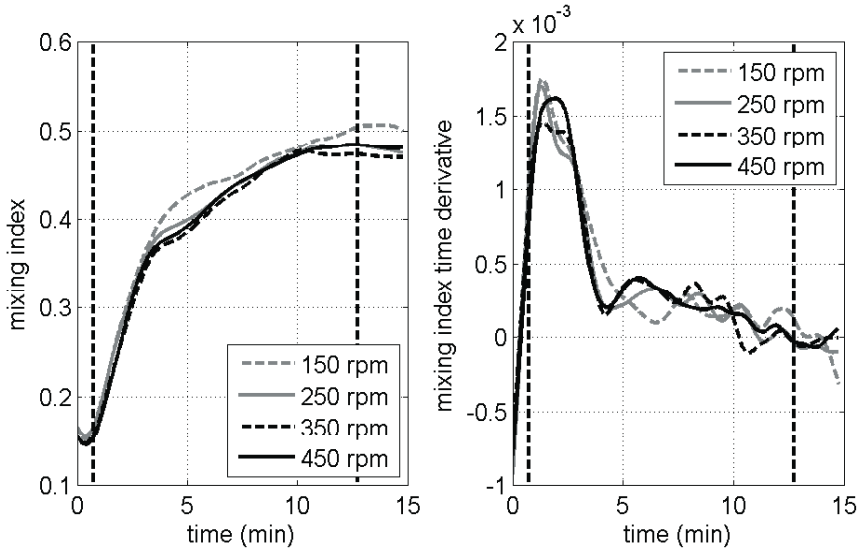

Figure 3.5: The smoothed mixing index curves and their time derivatives from the granulation experiments. The dashed vertical lines are placed at time points when the liquid addition is turned on and off, respectively. It was found that the mixing index levelled off (time derivative approached zero) at the end of the successful granulations.

3.1.4 Summary

The analysis of the high-shear granulations suggests that the mixing index and its time derivative could be used for monitoring the progress of granulation. The mixer shaft in the middle of the sensor could be taken into account with the help of boundary conditions in the ECT computations.

3.2 STUDY 2: FLUIDIZED-BED DRYING OF PHARMACEUTICAL GRANULES

In this study, the moisture and the hydrodynamics of pharmaceutical granules during fluidized bed drying were monitored with 3D electrical capacitance tomography. This work was presented in Publication **II**.

3.2.1 Methods

The fluidized-bed set-up that was used in the experiments is shown in figure 3.6. The fluidizing air was supplied by a rotary blower (Effepizeta, SCL V4), the air was heated with an air preheater (Watlow, CBEN24G6-21) and the air temperature was controlled with a PID logic controller (Watlow series 935A). The temperature of the air was kept at 40°C in all of the experiments. The air flow was monitored with a water manometer and controlled with two bypass valves. The humidity of the input air in the drying experiments was between 34–38 %.

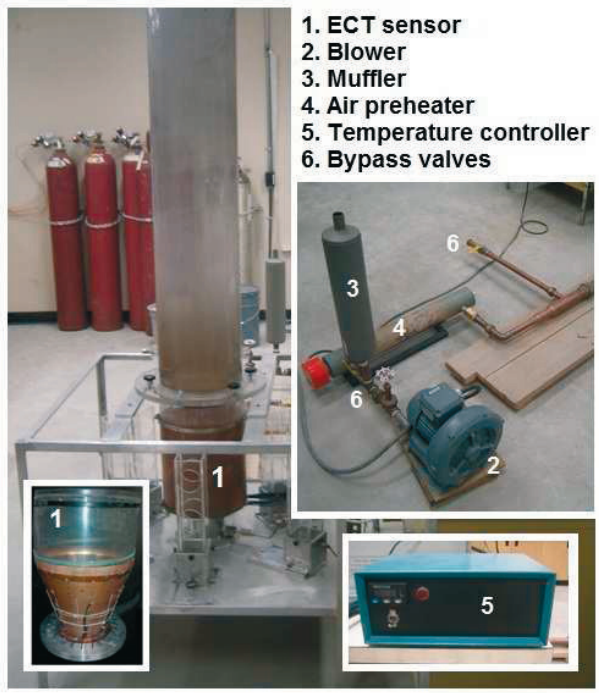

Figure 3.6: The fluidized-bed set-up used in this research.

The ECT sensor that was used consisted of a plexiglass product bowl, four layers of electrodes with eight trapezoidal electrodes on each layer, and an external copper screen. The lowest two electrode layers were used for measurements, the two uppermost layers were

electrically grounded during the measurements (see figure 3.7). The electrodes were installed on the outer surface of the bowl.

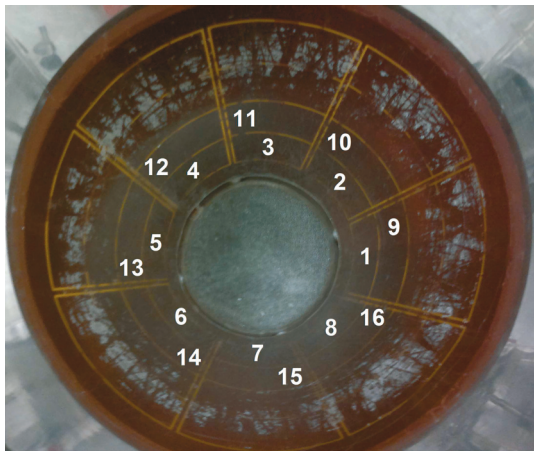

Figure 3.7: The interior of the product bowl with the electrode numbering used in this study. The two lowest electrode layers were used for measurements, and the two uppermost layers were electrically grounded during measurements.

PTL300 with data acquisition module DAM-200 (Process Tomography Ltd.) was utilized to gather the absolute values of the capacitances. The measurement device was actually designed for two-dimensional tomography, even though it was used here for 3D tomography. This involved having two electrodes being excited simultaneously. The electrode connections are explained in table 3.1. First, the electrodes corresponding to channel M1 on both planes were excited, and then all the independent capacitances (or electric charges) were measured among the electrodes connected to plane 1 and among the electrodes connected to plane 2 (i.e. neither the reciprocal capacitances nor the inter-plane capacitances were measured). The next excitation electrodes were the ones connected to channels M2. The simultaneous excitation of two electrodes was taken into account in the computations with the help of boundary conditions. For example, the resulting sensitivity distribution when two electrodes are excited is shown in figure 3.8, and for comparison the distribution when only one electrode is excited is also

shown.

Table 3.1: The connection table of electrodes to the measurement channels. The column numbers represent the measurement channels on each measurement plane, and the row numbers represent the two measurement planes. The numbers in the cells are the ordinal numbers of the electrodes as defined in figure 3.7.

	Channels							
	M1	M2	M3	M4	M5	M6	M7	M8
Plane 2	9	2	11	4	13	6	15	8
Plane 1	1	10	3	12	5	14	7	16

An inhouse image reconstruction algorithm was used to estimate 3D moisture distributions. It utilized the difference reconstruction method explained in section 2.1.2 and an experimentally determined mapping between the moisture and the relative permittivity of the material. During the drying experiments, the relative permittivity of the material changed radically: at the beginning it was more than 20 and at the end less than 2. This can be taken into account either by calibrating the ECT device during the experiments [65,67,68,135] or by modifying the computations. Here, the latter option was chosen: the linearization point (which was also the reference point) of the difference reconstruction algorithm was changed during the drying according to the measurement data.

3.2.2 Materials and experiments

Pharmaceutical placebo materials for tablets were used in the experiments. Microcrystalline cellulose (31.0 % of the wet granule mass) and lactose (35.2 %) were the filler materials, croscarmellose sodium (1.4 %) was the disintegrant and hydroxypropyl methylcellulose (2.8 %) was the binder. In addition, reverse osmosis water (29.6 %) was used as the liquid. The dry materials were mixed with a low-shear mixer (Kitchen-Aid Classic mixer), and the water was introduced with a peristaltic pump (VWR Scientific). The final product was sieved through a 3.36 mm screen to remove large

particles. In each of the experiments, 2 kg of wet granules were used. First, the relationship between granule moisture and relative permittivity was determined, and it is shown in figure 3.9.

In the drying experiments, ECT data was recorded at 7 minute intervals, and also small samples for reference moisture measurements were taken from the middle of the bed after each 7 minutes. The moisture was determined with a moisture analyzer (Mettler-Toledo HB43 drying balance).

Three experiments were carried out. The superficial gas velocity v_{dist} was varied in the experiments, and it was defined as the average velocity across the inlet to the conical section (at the distributor level). In the first experiment, the superficial gas velocity was 1.96 m/s at the start, after 23 minutes it was reduced to 1.68 m/s, and after a further 5 minutes to 1.05 m/s. The total duration of the first experiment was 42 minutes. The reduction of the air velocity during the experiments was carried out because the driest and smallest granules started to become entrained in the air stream and flow out from the fluidized-bed.

In the second experiment, the superficial gas velocity was initially 1.68 m/s, and after 30 minutes it was reduced to 1.05 m/s. The total duration of the second experiment was 49 minutes.

In the third experiment, the initial superficial gas velocity was 1.68 m/s; after 7 minutes it was reduced to 1.05 m/s. A higher velocity was needed in the beginning to promote good mixing. The total duration of the third experiment was 63 minutes.

3.2.3 Results and discussion

The 3D moisture distribution of the wet granules was computed. In order to estimate the average moisture content, the effect of the fluidizing air had to be taken into account. This was because the ECT device ultimately responded to changes in the relative permittivity distribution, and air has a lower relative permittivity ($\epsilon_r \approx 1.0006$) than the wet granules. Therefore, as the air flowed through the wet granules, the effective permittivity observed by the ECT could be

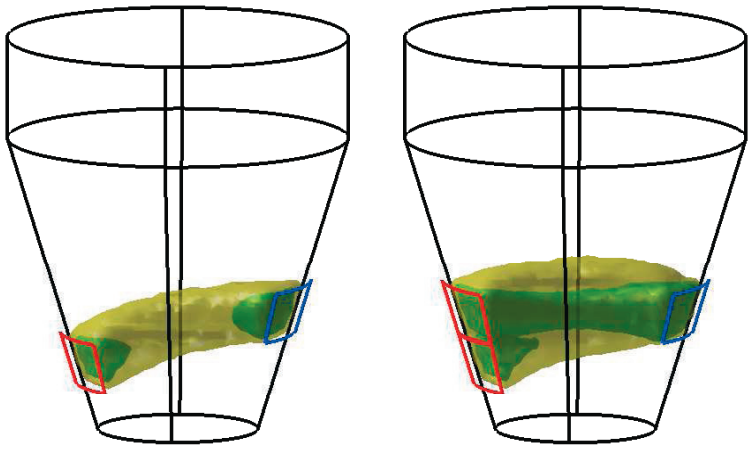

Figure 3.8: Isosurfaces of the sensitivity distribution when the charge of the opposite electrode is measured. The excitation electrodes are colored red (black in gray scale figure), and the grounded sensing electrode is colored blue (gray). The yellow (light gray) isosurface corresponds to the sensitivity value -7×10^{-7} *Vm and the green (dark gray) the value* -2×10^{-6} *Vm.*

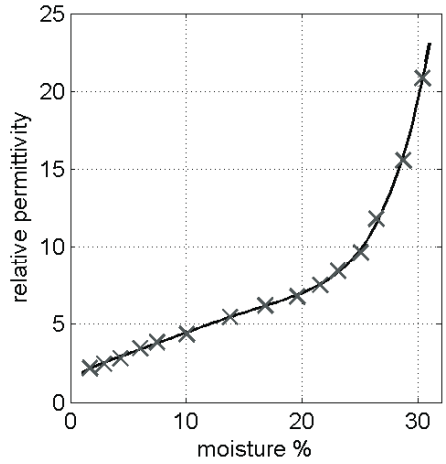

Figure 3.9: The data (crosses) presents the moisture values determined from small samples taken during drying and the corresponding estimated homogenous permittivities. The fifth order fitting polynomial (line) is of the form $\epsilon_r = 5.2186 \times 10^{-6}\chi^5 - 2.7991 \times 10^{-4}\chi^4 + 0.0055\chi^3 - 0.0487\chi^2 + 0.4640\chi + 1.4679$.

lower in certain locations than the actual permittivity of the wet material, and thus also the reconstructed moisture values were lower than the actual moisture values of the wet material.

Therefore in the estimation of the average moisture content, thresholding was used. This meant that only the moisture values above a certain threshold value were used in the estimation. Here, the thresholding value was chosen to be the mean value of the whole moisture distribution, and the thresholded moisture estimator was the mean of the moisture values above this threshold. The first row of figure 3.10 shows the thresholded moisture estimates and the reference results from the small samples. The timepoints when the linearization point was changed are shown with vertical solid lines, and the dashed vertical lines depict the timepoints when the superficial air velocity was adjusted. The thresholded moisture estimate works very well in comparison to reference results, although the moisture values at high velocities are slightly underestimated and furthermore there are some overestimated moisture values around 10–15 %.

The second row in figure 3.10 presents a moisture estimate based on the moisture values near to the walls of the product bowl. It was hypothesized that at most of the time there would be some material located at the edges. The result is rather similar to the thresholded moisture value; however, there is less overestimated moisture values around 10–15 %.

Figure 3.11 shows 3D moisture distributions when the moisture content of the granules was 15 % (determined from the reference moisture curves). Only the volume that was covered by the measurement electrodes is shown in the figure. The figures represent the average behaviour of the bed during one minute time periods. The top rows of figures, 3.11(a)-(c), present three 2D slices from the distribution, the middle rows, 3.11(d)-(f), 2D vertical cross-sections and the bottom rows, 3.11(g)-(i), 3D constant moisture surfaces which enclose a volume that contains moisture values higher than the moisture value mentioned above the figure.

The distributions corresponding to different air velocities look

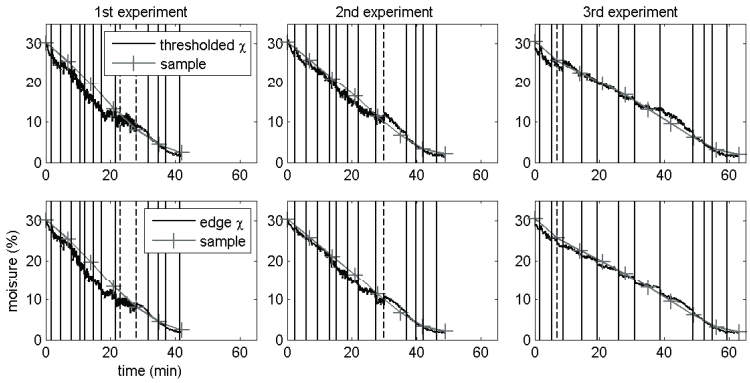

Figure 3.10: The reference moisture values (gray crosses) and two different estimates (black curves) of the moisture of the wet granules with respect to time during the drying experiments. The solid vertical lines denote the time points when the linearization point was changed and the dashed vertical lines when the air flow was adjusted.

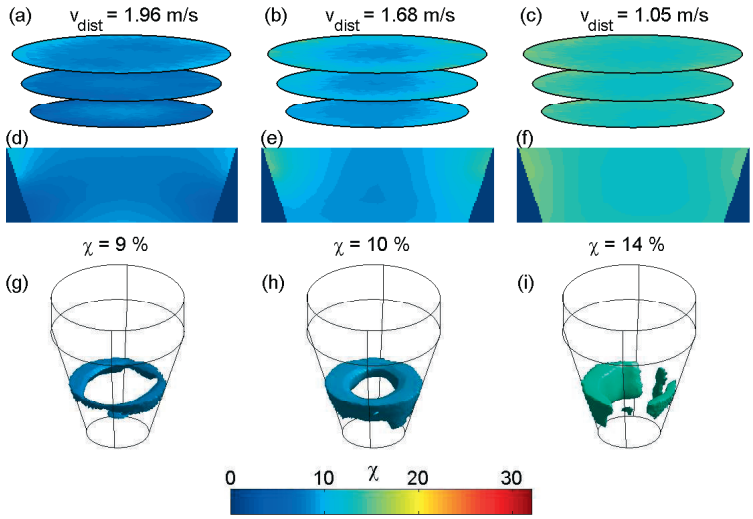

Figure 3.11: Different visualizations of the three-dimensional moisture distribution from one minute of measurements around 15 moisture percent: (a)-(c) represent 2D slices from the 3D moisture distributions; (d)-(f) represent vertical cross-sections from the distribution; (g)-(i) represent constant moisture surfaces corresponding to values 9 %, 10 % and 14 %, respectively.

dissimilar, and some of the moisture values are much less than the nominal 15 %. In order to understand why this is the case, one must bear in mind that the distributions are averages of both wet granules and voids going through the bed during one minute of time. Taking this consideration into account and by examining the reconstructed moisture values, one can conclude that the obvious explanation is that there were more voids going through the granules when the air velocity was high. The distributions corresponding to velocities 1.96 and 1.68 m/s contain moisture values much lower than 15 %, this is evident especially at $v_{\text{dist}} = 1.96$ m/s.

In figure 3.12, the bed behaviour is presented with respect to time at all of the studied air velocities and when the granule moisture is 15 %. The pictures on the left contain 2D cross-sections taken between the electrode levels and show them as being stacked one below the other with respect to time (the time axis is drawn from top to bottom). The constant moisture surfaces in these so-called time pipes enclose the moisture values higher than 15 %. The pictures in the middle depict lines across the diameter of the 2D cross-sections stacked one below the other with respect to time, and the pictures on the right represent the normalized moisture curves. The curves were calculated by first normalizing each of the time pipes with the help of the highest moisture value (within each time pipe) and then by calculating an average of the normalized moistures at each time point. In general terms, the normalized moisture curve could also resemble the solid fraction curve because in both curves, voids can be seen as small values and moist solid materials as high values.

As can be seen from figure 3.12, at the two highest velocities there were much more voids present and therefore the normalized moisture curve shows a clearly periodical behaviour and high amplitudes. The voids are much larger and seem to move mostly near to the walls, although some voids appear to cover nearly the whole diameter of the bowl which can also be seen from the normalized moisture curve as values close to zero. The constant moisture surfaces enclosed less material when the air velocity was 1.96 m/s than

when it was 1.68 m/s. It seems that there were less variations in the moisture distributions in the middle of the bowl than near to the walls. With the lowest air velocity, the bed behaviour near the walls was rather stable, there were small voids going through both the middle and near the walls, and the normalized moisture curve did not have as high amplitudes.

Since the absolute moisture is normalized out from the normalized moisture curves and the curves describe the overall behaviour of the bed, they were examined in greater detail. In figure 3.13, the mean values and the standard deviations of these curves are presented with respect to the absolute moisture at the three air velocities.

The figures show that as the granules dried, the mean of the normalized moisture decreased and the standard deviation increased. At the beginning at high moisture values, channeling behaviour could be observed, and this could be seen as a stable normalized moisture curve which had a high mean value and a low standard deviation. As the granules dried, the bed behaviour changed and the voids started to move through the bed which could be seen as a periodical normalized moisture curve with a clear amplitude. For this reason, the mean normalized moisture started to decrease and the standard deviation to increase. As the granules dried even further, the size of the voids increased which could be seen as lower normalized moisture values on average and as higher amplitudes in the curve: therefore, the mean value further decreased and the standard deviation increased. At one point, the fluidizing air started to entrain fine particles from the bed. At this point, both the mean value and the standard deviation of the normalized moisture curve began to plateau.

Based on the previous explanation, both the mean value and the standard deviation of the normalized moisture characterize the hydrodynamic properties of the wet granules during drying. From a monitoring point of view, if one is attempting to maintain a stable hydrodynamic state as the granules dry, one should monitor both of these curves and adjust the air flow in such way that both curves

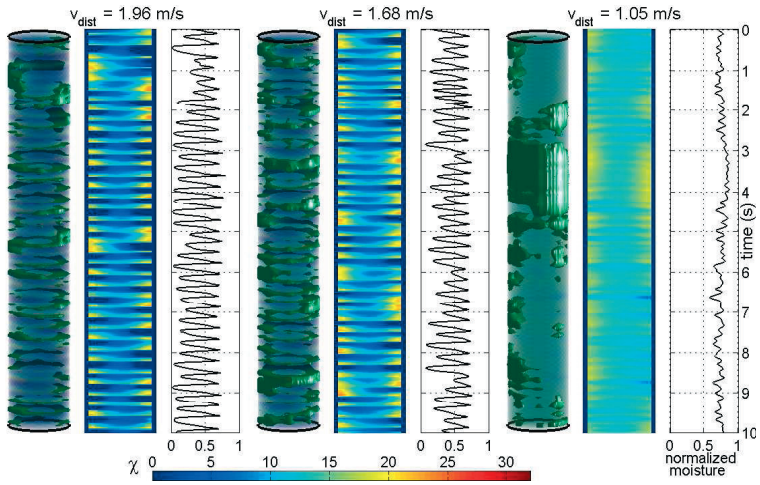

Figure 3.12: Visualizations from the moisture distributions with respect to time when the bed moisture was around 15 %. The pictures on the left represent time pipes and constant moisture surfaces enclosing moisture values higher than 15 %. The pictures in the middle represent lines across the diameter of the time pipes. The pictures on the right represent the normalized moisture curves.

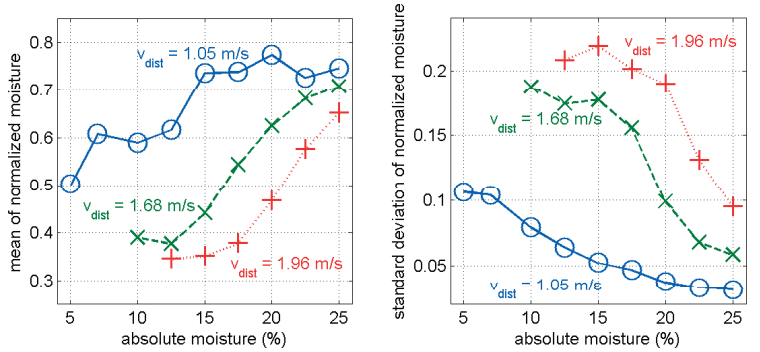

Figure 3.13: The mean and the standard deviation of the normalized moisture with respect to the absolute moisture content when different superficial air velocities were used.

remain at a desired constant level.

3.2.4 Summary

In fluidized bed drying, the thresholded moisture estimate and the moisture values near to the edge of the bowl could be used for monitoring the moisture of the granules, and the mean value and the standard deviation of the normalized moisture curve could be used for monitoring the hydrodynamics. The ECT equipment originally designed for two-dimensional tomography could be used for three-dimensional tomography by taking into account the simultaneous excitation of the two electrodes in the computations.

3.3 STUDY 3: DISSOLUTION TESTING OF PHARMACEUTICAL TABLETS

This section reviews results of the drug release monitoring from pharmaceutical tablets with the help of 3D EIT. The work was presented in Publications **III** and **IV**: in Publication **III**, the measurement procedure was described, the EIT computations were detailed and the technique was demonstrated with sodium chloride (NaCl) tablets; in Publication **IV**, the accuracy of the technique was evaluated and the characteristics of the technique were described.

3.3.1 Methods

The experimental set-up is shown in figure 3.14. It resembled the USP dissolution II apparatus: the set-up consisted of a dissolution vessel (AT6 vessel, Sotax), electrically insulating paddle (TPD016-02 Distek) and an electronic overhead stirrer (RZR 2102 control Z Heidolph). The vessel was modified by attaching 80 electrodes through its surface. The electrodes were arranged in five arrays each consisting of 16 electrodes. Weak alternating electric currents (frequency 10 kHz and amplitude 0.5 mA) were injected through the electrodes as shown in table 3.2. An EIT instrument that was engineered inhouse [119] measured voltages from the electrodes with the help of

a light port trigger introduced in order to keep track of the paddle orientation.

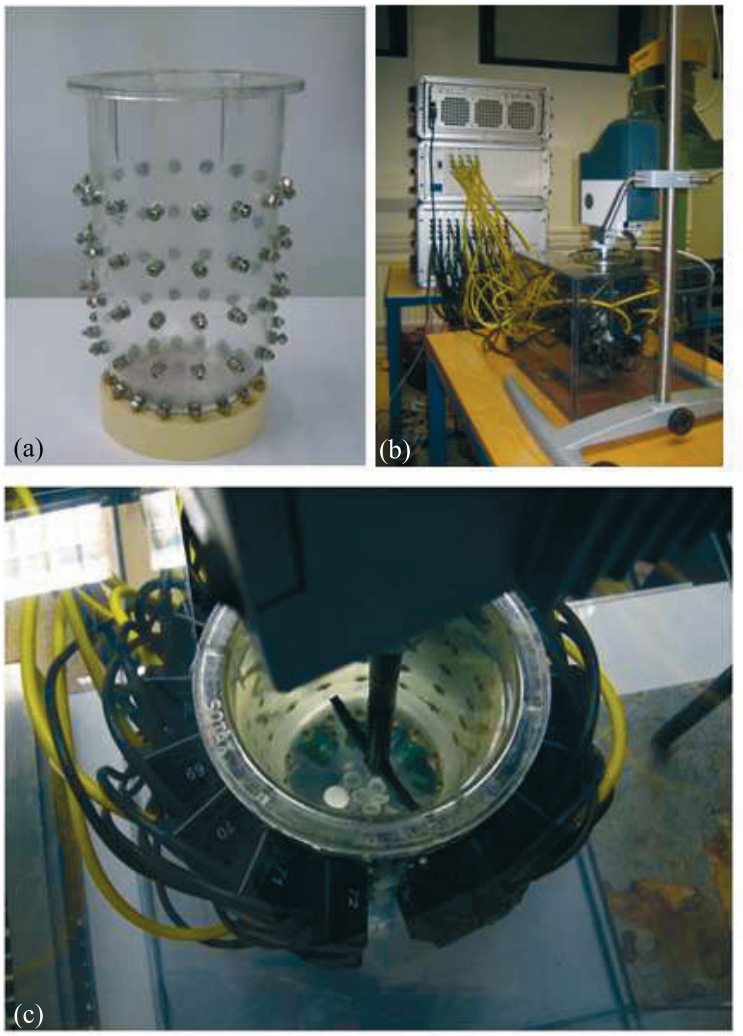

Figure 3.14: (a): The modified dissolution vessel with 80 electrodes. (b): Experimental set-up with the EIT instrument in the back, the vessel and the overhead stirrer in the front. (c): Close-up of the vessel with a tablet at the bottom.

Table 3.2: The current injection protocol. The column numbers represent the 16 electrodes on each array, and the row numbers represent the five horizontal arrays. The figures in the cells are the ordinal numbers of the current injections. The electrodes of the first current injection are denoted by circles.

		Electrode															
		1	2	3	4	5	6	7	8	9	10	11	12	13	14	15	16
Array	5																
	4			4				8				3				7	
	3	2				6				①				5			
	2			3				7				4				8	
	1	①				5				2				6			

The inhouse 3D-EIT reconstruction method described in section 2.2.2 was used to estimate both the concentration distribution and contact impedances of the electrodes at each time point. The concentration distribution was computed through an experimentally determined mapping between the drug concentration and the electric conductivity. The reason why the simultaneous estimation of contact impedances was essential can be seen from figure 3.15. The figure is drawn from an experiment which was carried out with a tablet containing sodium chloride (NaCl) and it displays two vertical cross-sections of the estimated NaCl concentration distribution at $t = 1$ min. The cross-section on the left is computed using the simultaneous contact impedance estimation and the cross-section on the right is computed without the contact impedance estimation. From the cross-section on the left, one can see that the concentration distribution is relatively homogenous throughout the vessel; the concentration values at the bottom of the vessel are slightly higher than at the top. This supports previous results that the vessel should always be well mixed [38]. From the cross-section on the right, one can see that there are clear artefacts near to the current carrying electrodes. The artefacts are due to changes in contact impedance values during the process.

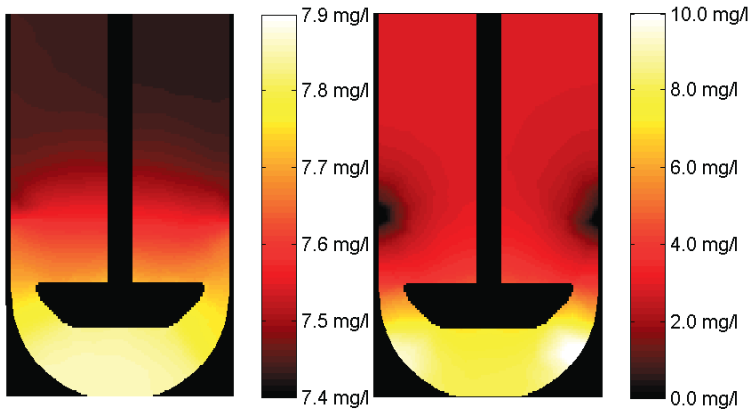

Figure 3.15: Left: The NaCl concentration distribution at $t = 1$ min when the reconstruction algorithm estimates both the concentrations and the contact impedances. Right: The same distribution when the simultaneous estimation of contact impedances was omitted.

3.3.2 Materials and experiments

Five tablets containing propranolol hydrochloride (S.I.M.S.) (74 % of the total weight) as the releasing ingredient and potato starch acetate (Polymer Corex Oy Ltd.) (26 %) as the matrix former were used. Propranolol hydrochloride was chosen because its release increased the conductivity of the dissolution medium, and starch acetate because it did not dissolve nor did it change the conductivity of the medium. The tablets were compacted with a compaction simulator (PCS-1 Puuman Ltd.) to produce cylindrical tablets that would disintegrate during testing. The dissolution medium was made from 10 l of outgassed deionized water by adding 850 g of sodium chloride. The volume of the medium was 1.2 l and it was held in room temperature (20°C). First, the relationship was determined between the propranolol hydrochloride concentration in the dissolution medium and conductivity; it is shown in figure 3.16.

Next, five drug release experiments were conducted one after another. In each experiment, a tablet was dropped into the vessel, the paddle rotated 50 rpm, and EIT measurements were carried out for 150 minutes.

3.3.3 Results and discussion

Figure 3.17 presents the three-dimensional drug concentration distributions of the first tablet experiment at $t = 5\,\text{min}$, $t = 60\,\text{min}$ and $t = 120\,\text{min}$. Moreover, there are isosurfaces corresponding to certain constant concentrations. The shapes of the distributions are similar which is due to the fact that the paddle rotation speed is kept constant. The isosurfaces near the bottom are somewhat round, whereas the isosurfaces above the paddle blade are more flat.

There seem to be changes in the homogeneity with respect to time: the difference between the maximum and the minimum value of the distribution is 17.0% of the mean value at $t = 5\,\text{min}$, 9.0% at $t = 60\,\text{min}$ and 6.8% at $t = 120\,\text{min}$. Since the blending conditions stay the same, the difference is probably due to the changes in the drug release rate.

Figure 3.18(a)-(e) present the drug release curves calculated from the concentration distribution with the help of the equation

$$m_t = \int_\Omega c_t(\boldsymbol{x})\mathrm{d}\boldsymbol{x}, \tag{3.1}$$

where m_t is the total mass of the released drug at time point t, c_t the estimated concentration distribution and Ω the computational domain. The crosses are from reference measurements that were carried out with the help of small samples taken from the medium and a UV/VIS spectrophotometer (Genesys 10 UV Thermo Spectronic). Furthermore, figure 3.18(f)-(j) shows the time derivatives of the release curves, i.e., the drug release rates.

The tablets disintegrated into smaller pieces during the experiments, and this can be seen as slope increases in the release curves (solid lines in figures 3.18(a)-(e)) which are calculated from the EIT data with the equation (3.1). First, all the tablets broke into two pieces, and some disintegrated later into even smaller pieces, which explains why some curves have more than one slope increase. In the rate curves, the disintegrations can be seen as sharp peaks. The time of the first breakage, for example, can be determined from the

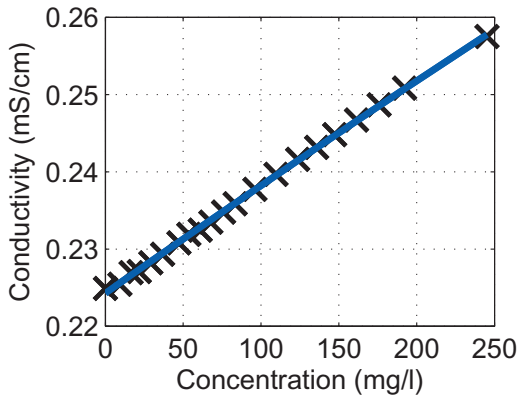

Figure 3.16: The relationship between drug concentration and conductivity was found to be $\sigma = g(c) = -1.8184 \cdot 10^{-8}c^2 + 1.4105 \cdot 10^{-4}c + 0.2243$.

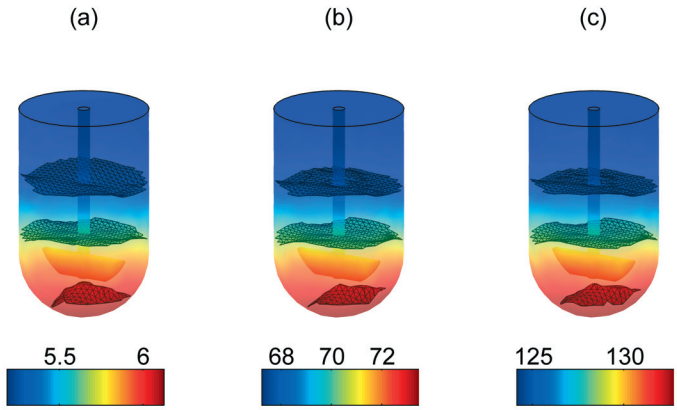

Figure 3.17: (a): The three-dimensional propranolol hydrochloride concentration distribution at $t = 5$ *min with three isosurfaces corresponding to 5.3, 5.7 and 6.1 mg/l. The unit of the colorbar is mg/l. (b): The distribution at* $t = 60$ *min and isosurfaces corresponding to 67.9, 70.4 and 73.3 mg/l. (c): The distribution at* $t = 120$ *min and isosurfaces corresponding to 125.1, 128.6 and 132.4 mg/l. The drug release test was performed in outgassed deionized water (*$20 \pm 1\,^{\circ}\mathrm{C}$*, NaCl concentration 85 mg/l) using the USP dissolution apparatus 2. The results are for tablet no. 1 (see figures 3.18(a) and 3.18(f)).*

EIT curves but not from the UV curves, which gives an impression of the better sensitivity and temporal accuracy that can be achieved with EIT monitoring.

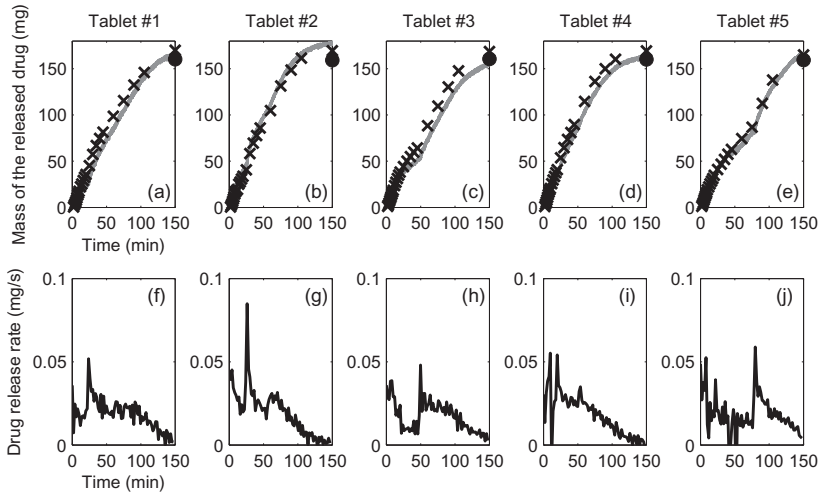

Figure 3.18: (a)-(e): Propranolol hydrochloride release curves from tablets in outgassed deionized water ($20 \pm 1\,^{\circ}\mathrm{C}$*, NaCl concentration* $85\,mg/l$*) using USP dissolution apparatus 2. The solid lines are calculated based on the integration formula (3.1), the crosses are from the UV/VIS spectrophotometric analysis, and the dots are the total masses of the propranolol hydrochloride determined from the tablets' weights. (f)-(j): Propranolol hydrochloride release rates. The tablet disintegrations can be seen as sharp rate increases.*

In order to analyze the accuracy, the drug release results from EIT and UV/VIS spectrophotometer were compared with the help of the difference factor f_1. This factor is normally used to evaluate the difference between drug release properties of formulations and manufacturing batches [136]. Here, it is defined as

$$f_1 = \frac{\sum_{t=t_1}^{t_{N_s}} \left| m_t^{UV} - m_t^{EIT} \right|}{\sum_{t=t_1}^{t_{N_s}} m_t^{UV}} \times 100, \tag{3.2}$$

where, m_t^{UV} and m_t^{EIT} are the masses of the released substance based on the UV and EIT analysis, respectively, at time t, and N_s is the number of samples. The f_1 values for the tablets no. 1-5 were 16.9, 11.3, 13.7, 11.1 and 7.5, respectively. The smaller the f_1

value, the better is the consistency, and in practice, profiles are considered similar if $f_1 \leq 15$. Taking into account that these values were obtained from the comparison of two different measurement techniques (not two different tablets), the values are very good.

3.3.4 Summary

In drug release testing, it was shown that accurate drug release curves and drug release rates could be calculated based on the tomograms. The changes in the contact impedance values of the electrodes during the process could be taken into account by estimating both the contact impedance values and the concentration distribution simultaneously as a function of time.

4 Conclusions and future work

In this thesis, electrical tomography imaging was used to monitor high-shear granulation, fludized-bed drying and drug release testing. In each of the studies, various technical and computational approaches were developed to make possible the implementation of the selected electrical imaging modality possible. Different ways to use the tomograms for producing appropriate monitoring signals were proposed. The applicability in each study was demonstrated with realistic materials and experimental conditions. In the following sections, benefits and shortcomings related to the techniques and their implementation will be presented, and finally some future prospects will be described.

4.1 BENEFITS

Spatial and temporal information: Electrical tomography techniques provide more spatial information when compared to many other commonly used techniques such as conductivity probes, NIR probes, acoustic emission, pressure measurements and microwave measurements. While other techniques tend to provide pointwise information, ECT and EIT are able to provide the user with for example 2D- or 3D-tomograms of the target. Furthermore, processes like high-shear granulation and fluidized-bed drying are very fast and sometimes chaotic and under these conditions the good temporal resolution of ECT and EIT is as important as the spatial information. In drug release testing, substances that dissolve rapidly (i.e. in less than 30 s which is the blend time to achieve 95 % uniformity level in the USP dissolution apparatus II [38]) cannot properly be characterized with other techniques: even if other methods did have the necessary temporal resolution they would not exhibit the spa-

tial resolution that is needed to take into account all the released drug since the mixing properties of the USP apparatus II are not sufficient to blend the drug into the liquid homogeneously.

Non-invasiveness and non-intrusiveness: In pharmaceutical processes, sampling is a commonly used method to characterize the processed materials. However, the representativeness of the sample and the sampling method are often problematic. This is not a problem with ECT and EIT since no sampling is needed; all the measurements are made non-invasively and non-intrusively. Moreover, the process does not need to be stopped while measurements are made. Instrumentation of measurement probes for example inside fluidized-bed reactor can change the hydrodynamics and especially with wet materials, contamination of the probe can be a problem.

In-line monitoring: The reconstruction algorithms can be applied in-line which enables real time controlling. In these studies, the difference reconstruction method was applied which requires only one matrix-vector multiplication since all time-consuming pre-computations can be carried out beforehand. Moreover, to speed-up even further the computations, several numerical methods have recently been developed. For example, with the help of the approximation error method [103, 105], the forward model can be reduced without losing of the spatial resolution. In addition, the use of other data reduction methods such as the principal component analysis (PCA) [137, 138] can speed-up the computations.

Customization: In this thesis, it was shown that electrical tomography techniques can be modified and adjusted for multiple purposes. For example, with correct forward modelling, the internal metallic shaft in high-shear granulation study could be taken into account, and in the fluidized-bed drying study, the ECT device designed for 2D tomography could be modified to permit 3D tomography. The rotating paddle in dissolution testing could be taken into account with the help of a light-port trigger and a proper computational mesh. Furthermore, the alteration of the contact impedances could be taken into account by simultaneously estimating the contact impedances as a function of time.

4.2 SHORTCOMINGS AND SUGGESTED IMPROVEMENTS

Spatial resolution: The spatial resolution of electrical tomography techniques is low for example when compared to X-ray tomography. The reason is that the electric field used in the measurements is a so-called *soft field*: the field lines bend according to the the material properties of the target in contrast to the *hard field* used in the X-ray tomography. The spatial resolution of ECT and EIT depends on many factors such as the size and number of electrodes, the accuracy of the measurement device, measurement noise, the accuracy of the forward model, the discretization of the meshes, studied target, prior information and reconstruction algorithm. As a rule of thumb, the resolution of the techniques is at best a few percent of the diameter of the target, and the sensitivity of the methods is better near to the electrodes than in the middle of the sensor.

In these studies, the difference reconstruction method was used as the reconstruction algorithm. However, if further spatial accuracy should be needed or if there is no possibility to measure the required reference data set, other methods like the iterative Gauss-Newton algorithm could be used. The spatial accuracy could be further improved by using the proper smoothness prior [99]. Moreover, in high-shear granulations, the accuracy of the 2D-tomograms could be improved by taking the rotating impeller correctly into account and by using the metallic shaft in the middle as a measurement electrode. In the fluidized-bed drying study, the accuracy could be improved by using an actual 3D-tomograph with a proper 3D-sensor and by taking the air velocity correctly into account.

Specificity and interpretation of results: In some cases, there is a lack of specificity i.e. there are multiple reasons that could cause the observed changes. This was noted especially during 2D-ECT monitoring of high-shear granulation: for example, the vertical movement of the granules caused changes in the tomograms. Here, the use of 3D-ECT would be highly beneficial. Another improvement for the high-shear and for the fluidized-bed study would be the use of a three-phase (gas-liquid-solid) model that could be imple-

mented with the help of Kalman filtering. Implementation of a drug release model might also improve the specificity of the drug release study. Another computational aid would be to use chemometrics to statistically formulate correlations between process parameters, monitoring quantities and the material properties of the end product.

Another way to improve the specificity would be to increase the amount of available information. This would require the use of more sophisticated measurement devices. For example, using multiple frequencies or even spectroscopy might help in separating different substances from each other: e.g. some materials might be more sensitive to certain frequencies than others. Furthermore, EIT could be used in a way that both conductivity and permittivity distributions would be reconstructed: some substances might be separated from the conductivity distribution and others from the permittivity distribution.

Materials: The used imaging modality and the studied materials need to be chosen accordingly in order to permit electrical imaging. The materials that are suitable for ECT imaging are usually insulating, and the presence of significant conductive components can ruin the data. The choice of ECT for monitoring of the high-shear granulation and fluidized-bed drying was logical, since insulating powders and air were present. Liquids usually have conductive properties, however in these studies, the presence of liquids (or moisture) did not seem to cause any major problems.

In some cases, there might be challenges if several insulating or conductive components were present. For example, this could happen in a high-shear mixer if there were two or several different dry powders present at the beginning of the experiment and the objective was to study the homogeneity of the powder mixture. One would need to have an observable contrast in the permittivities of these materials in order to make possible the monitoring. In dissolution testing, if several substances changed the conductivity of the medium during testing, it might be challenging to estimate the released mass of each substance. In these cases, multifrequency

ECT and EIT could be useful.

In EIT studies, both conductive and insulating materials can be present, but the presence of highly conductive and highly permittive materials can be problematic due to the limited measurement range of the devices. For example, during the drug release study, it was noted that the conductivity of the typical buffer solutions was very high, and that most of the drug substances that were examined in the preliminary tests did not cause any measurable changes in the conductivity. Therefore, an effort was made to choose the dissolution medium and the releasing drug substance in a way that the drug release could be observed: the medium was devised to be only weakly conductive, and the drug was chosen in such way that it was a salt form of a drug and therefore it increased the conductivity of the medium when it was released.

The range of permittivities and conductivities applicable for tomographic measurements can be made wider by improving the sensitivity and dynamics of the measurement devices and by designing the sensors so that they are optimal for the measurements.

4.3 FUTURE WORK

Algorithms: As already mentioned, the image reconstruction algorithms can be further improved in terms of both spatial accuracy and computational speed.

Scale-up: The high-shear granulation and fluidized-bed drying studies were carried out in laboratory scale. In order to make these techniques relevant in practice, a scale-up to the industrial-scale would be needed. The designing of a functional ECT sensor for industrial use could be a challenge because of the size requirements, even though sensors with diameters of 96 cm [139] and 150 cm [54] have been introduced. To compensate for the signal-to-noise-ratio, relatively large electrodes may need to be used which on the other hand could mean that there would be some loss of the vertical information.

An alternative would be to cover only a sector or a part of the

vessel wall with electrodes. For example, this could be sufficient for high-shear granulation if the process can be assumed as being homogeneous in the angular direction. One drawback would be the decreased sensitivity in the middle of the sensor, but this could be compensated for by inserting an internal electrode in the middle of the sensor [140, 141]. As already mentioned in section 2.4, another alternative in some cases would be to use a linear sensor and to reconstruct, for example, only a 1D depth profile.

Control: Correct monitoring is not sufficient if one wishes to assure product quality, a proper feedback loop to control the process parameters is needed as well. In high-shear granulation, the monitoring signals would be the mixing-index and its time-derivative, and the processing parameters would be the impeller speed and the liquid addition rate. In fluidized-bed drying, the correct monitoring signal for moisture would be either the thresholded moisture estimated or the edge moisture, and for hydrodynamics the mean value and the standard deviation of the normalized moisture curve. The processing parameters would be the velocity and temperature of the fluidizing air. Further research will be required to correctly connect the signals and the parameters with each other. Moreover, if other process variables such as the amount of used energy, the amount of processed materials, the time or the money spent are to be included, then an appropriate multivariable optimization functional would need to be formulated first. As an example, an operational controlling loop was demonstrated in [68].

Processing tools and parameters: ECT and EIT can be used for developing processing vessels and for studying appropriate processing parameters. In many cases, electrical tomography techniques can be used to experimentally evaluate the blending properties or the hydrodynamics. For example, EIT could be used in studying the blending properties of the dissolution basket apparatus or in developing a new apparatus.

Other processes: As described in the literature review (section 1.4), there are not that many pharmaceutical processes that have previously been studied with electrical tomography. Different flu-

idized-bed processes have been the most extensively studied, but there is still room left for further studies, especially related to fluidized-bed granulation and coating. Other possible processes could include oscillatory baffled crystallizers, powder-powder mixing, different drying processes such as spouted-bed, spray and freeze drying, dissolution in a miniature scale and perhaps even tableting.

Continuous processing: It can be predicted that in the future continuous processing will become more popular in the pharmaceutical industry. Setting up a continuous processing line can be a complex operation and sudden changes during manufacturing can cause interruptions in the entire line. Therefore, it can also be predicted that electrical tomography techniques will become more common in monitoring of complex processes in the pharmaceutical industry and beyond.

5 Appendix: Finite element method -approximation of the 3D-ECT forward problem

This appendix describes how to compute the electric potential distribution, elecric charges at the electrodes and the Jacobian matrix in three-dimensional ECT. This appendix is written assuming that the Finite element method (FEM) -approximations have been made in the nodal-basis with tetrahedral elements.

5.1 ELECTRIC POTENTIAL DISTRIBUTION

The electric potential distribution u is solved from the Poisson equation

$$\nabla \cdot \epsilon(\boldsymbol{x}) \nabla u(\boldsymbol{x}) = 0. \tag{5.1}$$

First, the weak variational form of equation (5.1) is formulated by multiplying the equation with a test function v and by integrating the equation over the domain Ω

$$\int_{\Omega} v \nabla \cdot \epsilon \nabla u \, \mathrm{d}\boldsymbol{x} = 0. \tag{5.2}$$

Next, using the Green's formula, the equation (5.2) can be written in the form

$$\int_{\partial\Omega} v \epsilon \frac{\partial u}{\partial \boldsymbol{\nu}} \, \mathrm{d}S - \int_{\Omega} \epsilon \nabla u \cdot \nabla v \, \mathrm{d}\boldsymbol{x} = 0. \tag{5.3}$$

Here, $\boldsymbol{\nu}$ is the outward unit normal vector. The boundary $\partial\Omega$ can be divided into two parts: the boundary with known boundary potentials is denoted with $\partial\Omega_b$ and the boundary with unknown boundary potentials as $\partial\Omega \setminus \partial\Omega_b$

$$\int_{\partial\Omega_b} v \epsilon \frac{\partial u}{\partial \boldsymbol{\nu}} \, \mathrm{d}S + \int_{\partial\Omega \setminus \partial\Omega_b} v \epsilon \frac{\partial u}{\partial \boldsymbol{\nu}} \, \mathrm{d}S - \int_{\Omega} \epsilon \nabla u \cdot \nabla v \, \mathrm{d}\boldsymbol{x} = 0. \tag{5.4}$$

In this study, the boundary $\partial\Omega_b$ consists of surfaces related to the electrodes and grounded screens. Here, the test functions are required to vanish where essential boundary conditions are prescribed, that is, $v(\boldsymbol{x}) = 0$ when $\boldsymbol{x} \in \partial\Omega_b$. Therefore, the first term of (5.4) is zero. The boundary $\partial\Omega \setminus \partial\Omega_b$ covers the rest of the surfaces, and a Neumann boundary condition $\epsilon \frac{\partial u}{\partial \boldsymbol{\nu}} = 0$ is set for this surface. Therefore, the second term of (5.4) is also zero, and (5.4) obtains the form

$$\int_\Omega \epsilon \nabla u \cdot \nabla v \, \mathrm{d}\boldsymbol{x} = 0. \tag{5.5}$$

For the FEM computations, the domain Ω is divided into N_E disjoint elements joined at N nodes. The permittivity and potential can be discretized respectively as

$$\epsilon(\boldsymbol{x}) = \sum_{i=1}^{n} \epsilon_i \phi_i(\boldsymbol{x}), \tag{5.6}$$

$$u(\boldsymbol{x}) \approx u_h(\boldsymbol{x}) = \sum_{i=1}^{N} u_i \varphi_i(\boldsymbol{x}), \tag{5.7}$$

where $\phi(\boldsymbol{x})$ are the chosen basis functions for permittivity, usually piecewise constant of piecewise linear basis functions are used. Moreover, $\varphi_i(\boldsymbol{x})$ are the nodal basis functions of the finite element mesh, and $u_h(\boldsymbol{x}) \in H_h = \operatorname{span}\{\varphi_i \mid 1 \leq i \leq N\}$ which is a subspace of $H^1(\Omega)$. It is denoted that $\boldsymbol{\epsilon} = [\epsilon_1, \epsilon_2, \cdots, \epsilon_n]$ is the vector representation of $\epsilon(\boldsymbol{x})$ and $\boldsymbol{u} = [u_1, u_2, \cdots, u_N]$ is the vector representation of $u_h(\boldsymbol{x})$.

Furthermore, it is denoted that the subdomain $\Omega \setminus \partial\Omega_b$ contains N_I nodes and the boundary $\partial\Omega_b$ with known potential values contains N_b nodes. The test functions are sorted in such way that indices $1 \leq i \leq N_I$ refer to subdomain $\Omega \setminus \partial\Omega_b$ and indices $(N_I + 1) \leq i \leq N$ to boundary $\partial\Omega_b$. By inserting the approximative functions into the variational form (5.5), and by choosing the test functions appropriately, the following matrix equation is obtained

$$\boldsymbol{A}\boldsymbol{u} = \boldsymbol{B} \tag{5.8}$$

where $\boldsymbol{A} \in \mathbb{R}^{N \times N}$ is the FEM matrix, $\boldsymbol{u} \in \mathbb{R}^N$ is the solution vector and $\boldsymbol{B} \in \mathbb{R}^N$ contains the boundary conditions. The matrix $\boldsymbol{A}$ has

the form

$$\boldsymbol{A} = \begin{bmatrix} \boldsymbol{A}_{N_I} \\ \boldsymbol{A}_b \end{bmatrix}. \tag{5.9}$$

Here, $\boldsymbol{A}_{N_I}$ is a $N_I \times N$ matrix and contains the rows that are associated with $\Omega \setminus \partial\Omega_b$, and it is of the form

$$\boldsymbol{A}_{N_I} = \begin{bmatrix} \int_\Omega \epsilon \nabla\varphi_1 \cdot \nabla\varphi_1 \mathrm{d}\boldsymbol{x} & \cdots & \int_\Omega \epsilon \nabla\varphi_N \cdot \nabla\varphi_1 \mathrm{d}\boldsymbol{x} \\ \int_\Omega \epsilon \nabla\varphi_1 \cdot \nabla\varphi_2 \mathrm{d}\boldsymbol{x} & \cdots & \int_\Omega \epsilon \nabla\varphi_N \cdot \nabla\varphi_2 \mathrm{d}\boldsymbol{x} \\ \vdots & \ddots & \vdots \\ \int_\Omega \epsilon \nabla\varphi_1 \cdot \nabla\varphi_{N_I} \mathrm{d}\boldsymbol{x} & \cdots & \int_\Omega \epsilon \nabla\varphi_N \cdot \nabla\varphi_{N_I} \mathrm{d}\boldsymbol{x} \end{bmatrix} \tag{5.10}$$

The nodes at the boundary $\partial\Omega_b$ are forced to the known potentials with the help of the matrix A_b which is of the size $N_b \times N$. The matrix A_b contains an $N_b \times N_I$ zero matrix and an $N_b \times N_b$ identity matrix

$$\boldsymbol{A}_b = \begin{bmatrix} 0 & 0 & \cdots & 0 & 1 & 0 & 0 & \cdots & 0 \\ 0 & 0 & \cdots & 0 & 0 & 1 & 0 & \cdots & 0 \\ \vdots & & \ddots & \vdots & \vdots & & \ddots & & \vdots \\ 0 & \cdots & & 0 & 0 & \cdots & & & 1 \end{bmatrix}. \tag{5.11}$$

The vector $\boldsymbol{B}$ is of the size $N \times 1$, and it contains an $N_I \times 1$ zero vector and the known potential values in vector $\boldsymbol{b}$ which is of the size $N_b \times 1$,

$$\boldsymbol{B} = \begin{bmatrix} 0 \\ \vdots \\ 0 \\ \boldsymbol{b} \end{bmatrix}. \tag{5.12}$$

Next, the solution vector u is computed as

$$\boldsymbol{u} = \boldsymbol{A}^{-1}\boldsymbol{B}. \tag{5.13}$$

Usually, the equation (5.13) is solved with the help of LU or QR decomposition, for example. Finally, the electric potential distribution is computed by inserting the $\boldsymbol{u}$ into equation (5.7).

5.2 ELECTRIC CHARGES

In a continous case, the electric charge at the lth electrode would be computed as

$$q_l(\epsilon) = -\int_{e_l} \epsilon(\boldsymbol{x}) \frac{\partial u(\boldsymbol{x})}{\partial \boldsymbol{\nu}} \mathrm{d}S \tag{5.14}$$

$$= -\int_{e_l} \epsilon(\boldsymbol{x}) \nabla u(\boldsymbol{x}) \cdot \boldsymbol{\nu} \mathrm{d}S. \tag{5.15}$$

The electric charges are computed for all the electrodes with the help of the discrete form of equation (5.15), the known permittivity distribution $\boldsymbol{\epsilon}$, the computed electric potential distribution $\boldsymbol{u}$ and a measurement operator that is denoted with $\boldsymbol{M}$. The measurement operator is a matrix of the size $N_e \times N$

$$\boldsymbol{M} = \begin{bmatrix} M_{11} & M_{12} & \cdots & M_{1N} \\ M_{21} & M_{22} & \cdots & M_{2N} \\ \vdots & & \ddots & \vdots \\ M_{N_e1} & M_{N_e2} & \cdots & M_{N_eN} \end{bmatrix}, \tag{5.16}$$

where N_e is the number of electrodes and N is the number of nodes in the finite element mesh. Here, the operator $\boldsymbol{M}$ is constructed electrode-wise as follows:

1. Choose one of the electrodes. Let it be denoted by e.

2. Pick a tetrahedral element that has one face on the electrode e. Denote the element as E_{ijkl} and the nodes at the electrode surface as $\boldsymbol{g}_i$, $\boldsymbol{g}_j$, $\boldsymbol{g}_k$. The node $\boldsymbol{g}_l$ completes the tetrahedron, but it is not on the surface (see figure 5.1).

3. Compute the outward unit normal vector $\boldsymbol{\nu}_{ijkl}$ and the area of the face a_{ijk} that is on the surface of the electrode. See details in section 5.2.1.

4. Compute the gradient operator ∇_{ijkl} related to the element. See details in section 5.2.2.

5. Calculate $(m_{ei}, m_{ej}, m_{ek}, m_{el}) = \nabla_{ijkl}^{\mathrm{T}} \boldsymbol{\nu}_{ijkl} a_{ijk}$.

6. Add these entries with the corresponding permittivity values to the matrix $\boldsymbol{M}$ as follows

$$M_{e(ijkl)} = M_{e(ijkl)} + (\epsilon(\boldsymbol{g}_i) m_{ei}, \epsilon(\boldsymbol{g}_j) m_{ej}, \epsilon(\boldsymbol{g}_k) m_{ek}, \epsilon(\boldsymbol{g}_l) m_{el}). \tag{5.17}$$

7. Go through all the elements that have one face on any of the sides of the electrode e repeating steps 2–6, and subsequently move on to the next electrode.

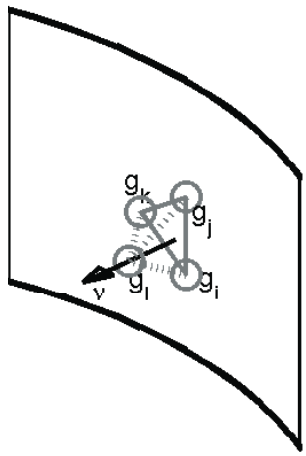

Figure 5.1: The nodes $\boldsymbol{g}_i$, $\boldsymbol{g}_j$ and $\boldsymbol{g}_k$ locate at the surface of an electrode and $\boldsymbol{g}_l$ locates off the surface. Here, the direction of the unit normal vector $\boldsymbol{\nu}$ is outwards from the surface.

Finally, the electric charges $\boldsymbol{Q}$ are computed as

$$\boldsymbol{Q} = -\boldsymbol{M}\boldsymbol{u}. \tag{5.18}$$

If all the electrodes have been covered when constructing the matrix $\boldsymbol{M}$, the electric charges at the excitation electrode is also computed. It is noteworthy that often the measurement devices do not provide data about the electric charge on the excitation electrode nor the data related to the reciprocal measurements.

5.2.1 The unit normal vector $\boldsymbol{\nu}_{ijkl}$ and the area a_{ijk}

Assume that nodes $\boldsymbol{g}_i$, $\boldsymbol{g}_j$, $\boldsymbol{g}_k$ and $\boldsymbol{g}_l$ form a tetrahedron element E_{ijkl} that has one surface on an electrode e, this surface which is a triangle is defined by nodes $\boldsymbol{g}_i$, $\boldsymbol{g}_j$ and $\boldsymbol{g}_k$, and the node $\boldsymbol{g}_l$ is off the surface (see figure 5.1),

$$\begin{pmatrix} \boldsymbol{g}_i \\ \boldsymbol{g}_j \\ \boldsymbol{g}_k \\ \boldsymbol{g}_l \end{pmatrix} = \begin{pmatrix} x_1^i & x_2^i & x_3^i \\ x_1^j & x_2^j & x_3^j \\ x_1^k & x_2^k & x_3^k \\ x_1^l & x_2^l & x_3^l \end{pmatrix}. \tag{5.19}$$

The normal vector is now calculated with the help of the cross product

$$\boldsymbol{\nu}_{ijkl} = \frac{(\boldsymbol{g}_k - \boldsymbol{g}_i) \times (\boldsymbol{g}_j - \boldsymbol{g}_i)}{\left\| (\boldsymbol{g}_k - \boldsymbol{g}_i) \times (\boldsymbol{g}_j - \boldsymbol{g}_i) \right\|}. \tag{5.20}$$

If a record has not been kept about the order and the locations of the nodes, it must be checked that the direction of the unit normal vector is outwards from the electrode surface.

Furthermore, the area of the triangle is

$$a_{ijk} = \frac{1}{2} \left\| (\boldsymbol{g}_k - \boldsymbol{g}_i) \times (\boldsymbol{g}_j - \boldsymbol{g}_i) \right\|. \tag{5.21}$$

5.2.2 The gradient operator ∇_{ijkl}

The computation of the gradient follows [102]. In general, the electric potential at point $\boldsymbol{x}$ can be presented as

$$u(\boldsymbol{x}) = c_0 + c_1 x_1 + c_2 x_2 + c_3 x_3. \tag{5.22}$$

Therefore, the gradient of the potential at the point is

$$\nabla u(\boldsymbol{x}) = (c_1, c_2, c_3)^{\mathrm{T}}. \tag{5.23}$$

Assume nodes as in section 5.2.1 and $\boldsymbol{x} \in E_{ijkl}$. Now the electric

potential at these nodes can be presented in a matrix form

$$\underbrace{\begin{pmatrix} 1 & x_1^i & x_2^i & x_3^i \\ 1 & x_1^j & x_2^j & x_3^j \\ 1 & x_1^k & x_2^k & x_3^k \\ 1 & x_1^l & x_2^l & x_3^l \end{pmatrix}}_{\boldsymbol{X}} \begin{pmatrix} c_0 \\ c_1 \\ c_2 \\ c_3 \end{pmatrix} = \begin{pmatrix} u^i \\ u^j \\ u^k \\ u^l \end{pmatrix}. \tag{5.24}$$

To solve the parameters $(c_0, c_1, c_2, c_3)^{\mathrm{T}}$, the inverse of $\boldsymbol{X}$ is needed. It is denoted as

$$\boldsymbol{X}^{-1} = \boldsymbol{R} = \begin{pmatrix} \boldsymbol{R}_0 \\ \boldsymbol{R}_1 \\ \boldsymbol{R}_2 \\ \boldsymbol{R}_3 \end{pmatrix}, \tag{5.25}$$

where $\boldsymbol{R}_0, \boldsymbol{R}_1, \boldsymbol{R}_2$ and $\boldsymbol{R}_3$ are the rows of $\boldsymbol{R}$. For the gradient, the three last rows are needed

$$\nabla u(\boldsymbol{x}) = \begin{pmatrix} c_1 \\ c_2 \\ c_3 \end{pmatrix} = \begin{pmatrix} \boldsymbol{R}_1 \\ \boldsymbol{R}_2 \\ \boldsymbol{R}_3 \end{pmatrix} \begin{pmatrix} u_i \\ u_j \\ u_k \\ u_l \end{pmatrix}. \tag{5.26}$$

Therefore, the gradient operator related to the element E_{ijkl} is

$$\nabla_{ijkl} = \begin{pmatrix} \boldsymbol{R}_1 \\ \boldsymbol{R}_2 \\ \boldsymbol{R}_3 \end{pmatrix}. \tag{5.27}$$

5.3 DERIVATION OF THE JACOBIAN MATRIX

The matrix representation of the kth row in the Jacobian matrix is computed here as follows

$$\begin{aligned}
\boldsymbol{J}_k &= \frac{\partial \boldsymbol{Q}}{\partial \epsilon_k} && (5.28)\\
&= \frac{\partial(-\boldsymbol{M}\boldsymbol{u})}{\partial \epsilon_k} && (5.29)\\
&= -\frac{\partial(\boldsymbol{M}\boldsymbol{A}^{-1}\boldsymbol{B})}{\partial \epsilon_k} && (5.30)\\
&= -\frac{\partial \boldsymbol{M}}{\partial \epsilon_k}\boldsymbol{A}^{-1}\boldsymbol{B} - \boldsymbol{M}\frac{\partial \boldsymbol{A}^{-1}}{\partial \epsilon_k}\boldsymbol{B} - \boldsymbol{M}\boldsymbol{A}^{-1}\frac{\partial \boldsymbol{B}}{\partial \epsilon_k} && (5.31)\\
&= 0 - \boldsymbol{M}\frac{\partial \boldsymbol{A}^{-1}}{\partial \epsilon_k}\boldsymbol{B} - 0 && (5.32)\\
&= \boldsymbol{M}\boldsymbol{A}^{-1}\frac{\partial \boldsymbol{A}}{\partial \epsilon_k}\boldsymbol{A}^{-1}\boldsymbol{B} && (5.33)\\
&= \boldsymbol{M}\boldsymbol{A}^{-1}\frac{\partial \boldsymbol{A}}{\partial \epsilon_k}\boldsymbol{u}, && (5.34)
\end{aligned}$$

The first term in (5.31) is not strictly speaking zero, since $\boldsymbol{M}$ depends on ϵ_k as can be seen from (5.17). However, the non-zero entries in matrix $\boldsymbol{M}$ correspond to nodes that are outside the region of interest and therefore they can be considered as constants and thus their derivative with respect to permittivity is zero. This argument was verified by computing another Jacobian matrix using the perturbation theory and comparing it with the Jacobian matrix computed using the presented method. The third term in (5.31) is zero because the boundary term $\boldsymbol{B}$ does not depend on ϵ_k.

Furthermore, the entries in $\partial \boldsymbol{A}/\partial \epsilon_k$ are of the form

$$\frac{\partial A_{ij}}{\partial \epsilon_k} = \begin{cases} \int_\Omega \phi_k \nabla \varphi_j \cdot \nabla \varphi_i \mathrm{d}\boldsymbol{x} & 1 \leq i, j \leq N_I \\ 0 & \text{otherwise.} \end{cases} \quad (5.35)$$

Again it is noteworthy, that often the measurement devices do not provide data about the electric charge of the excitation electrode nor data related to the reciprocal measurements. Therefore, the cor-

responding rows in the Jacobian matrix have to be removed when this kind of measurement data is used in the image reconstruction.

Bibliography

[1] F. J. Muzzio, T. Shinbrot, and B. J. Glasser, "Powder technology in the pharmaceutical industry: the need to catch up fast," *Powder Technol.* **124,** 1–7 (2002).

[2] U.S. Department of Health and Human Services Food and Drug Administration, "PAT - a framework for innovative pharmaceutical development, manufacturing, and quality assurance," (2004).

[3] D. C. Hinz, "Process analytical technologies in the pharmaceutical industry: the FDA's PAT initiative," *Anal. Bioanal. Chem.* **384,** 1036–1042 (2006).

[4] The Congress of the United States, Congressional Budget Office, "Research and development in the pharmaceutical industry," (2006).

[5] B. Shrestha, H. Basnett, P. M. Raj, S. S. Patel, M. Das, and N. K. Verma, "Process analytical technology: a quality assurance tool," *Research J. Pharm. Tech.* **2,** 225–227 (2009).

[6] S. M. Iveson, J. D. Litster, K. Hapgood, and B. J. Ennis, "Nucleation, growth and breakage phenomena in agitated wet granulation process: a review," *Powder Technol.* **117,** 3–39 (2001).

[7] S. M. Iveson, P. A. L. Wauters, S. Forrest, J. D. Litster, G. M. H. Meesters, and B. Scarlett, "Growth regime map for liquid-bound granules: further development and experimental validation," *Powder Technol.* **117,** 83–97 (2001).

[8] R. Ramachandran, J. M.-H. Poon, C. F. W. Sanders, T. Glaser, C. D. Immanuel, F. J. Doyle III, J. D. Litster, F. Stepanek, F.-Y.

Wang, and I. T. Cameron, "Experimental studies on distributions of granule size, binder content and porosity in batch drum granulator: Influences on process modelling requirements and process sensitivities," *Powder Technol.* **188,** 89–101 (2008).

[9] J. M.-H. Poon, R. Ramachandran, C. F. W. Sanders, T. Glaser, C. D. Immanuel, F. J. Doyle III, J. D. Litster, F. Stepanek, F.-Y. Wang, and I. T. Cameron, "Experimental validation studies on a multi-dimensional and multi-scale population balance model of batch granulation," *Chem. Eng. Sci.* **64,** 775–786 (2009).

[10] P. Kleinebudde, "Roll compaction / dry granulation: pharmaceutical applications," *Eur. J. Pharm. Biopharm.* **58,** 317–326 (2004).

[11] T. Schaefer, P. Holm, and H. G. Kristensen, "Melt granulation in a laboratory scale high shear mixer," *Drug Dev. Ind. Pharm.* **16,** 1249–1277 (1990).

[12] G. M. Walker, G. Andrews, and D. Jones, "Effect of process parameters on the melt granulation of pharmaceutical powders," *Powder Technol.* **165,** 161–166 (2006).

[13] H. G. Wang, T. Dyakowski, P. Senior, R. S. Raghavan, and W. Q. Yang, "Modelling of batch fluidised bed drying of pharmaceutical granules," *Chem. Eng. Sci.* **62,** 1524–1535 (2007).

[14] A. M. S. Costa and M. de Souza, "Comments on "Modelling of batch fluidised bed drying of pharmaceutical granules" - Chemical Engineering Science 62 (2007) 1524-1535," *Chem. Eng. Sci.* **65,** 5054 (2010).

[15] J. C. Cunningham, I. C. Sinka, and A. Zavaliangos, "Analysis of tablet compaction. I. Characterization of mechanical behavior of powder and powder / tooling friction," *J. Pharm. Sci.* **93,** 2022–2039 (2004).

[16] I. C. Sinka, J. C. Cunningham, and A. Zavaliangos, "Analysis of tablet compation. II. Finite element analysis of density distribution in convex tablets," *J. Pharm. Sci.* **93,** 2040–2053 (2004).

[17] A. Palmieri III, ed., *Dissolution theory, methodology, and testing* (Dissolution Technologies Incorporated, 2007).

[18] K. Plumb, "Continuous processing in the pharmaceutical industry: changing the mind set," *Trans. IChemE., Part A* **83,** 730–738 (2005).

[19] M. Bardin, P. C. Knight, and J. P. K. Seville, "On control of particle size distribution in granulation using high-shear mixers," *Powder Technol.* **140,** 169–175 (2004).

[20] G. Betz, P. Junker Bürgin, and H. Leuenberger, "Power consumption profile analysis and tensile strength measurements during moist agglomeration," *Int. J. Pharm. Sci.* **252,** 11–25 (2003).

[21] P. Luukkonen, M. Fransson, I. Niklasson Björn, J. Hautala, B. Lagerholm, and S. Folestad, "Real-time assessment of granule and tablet properties using in-line data from a high-shear granulation process," *J. Pharm. Sci.* **97,** 950–959 (2008).

[22] J. Rantanen, H. Wikström, R. Turner, and L. S. Taylor, "Use of in-line near-infrared spectroscopy in combination with chemometrics for improved understanding of pharmaceutical processes," *Anal. Chem.* **77,** 556–563 (2005).

[23] M. Whitaker, G. R. Baker, J. Westrup, P. A. Goulding, D. R. Rudd, R. M. Belchamber, and C. M. P., "Application of acoustic emission to the monitoring and end point determination of a high shear granulation process," *Int. J. Pharm.* **205,** 79–91 (2000).

[24] S. Watano, T. Numa, and Y. Osako, "A fuzzy control system of high shear granulation using image processing," *Powder Technol.* **115,** 124–130 (2001).

[25] L. Gradinarsky, H. Brage, B. Lagerholm, I. Niklasson Björn, and S. Folestad, "In situ monitoring and control of moisture content in pharmaceutical powder processes using an open-ended coaxial probe," *Meas. Sci. Technol.* **17,** 1847–1853 (2006).

[26] K. R. Morris, J. G. Stowell, S. R. Byrn, A. W. Placette, T. D. Davis, and G. E. Peck, "Accelerated fluid bed drying using NIR monitoring and phenomenological modeling," *Drug. Dev. Ind. Pharm.* **26,** 985–988 (2000).

[27] C. Buschmüller, W. Wiedey, C. Döscher, J. Dressler, and J. Breitkreutz, "In-line monitoring of granule moisture in fluidized-bed dryers using microwave resonance technology," *Eur. J. Pharm. Biopharm.* **69,** 380–387 (2008).

[28] F. Portoghese, F. Berruti, and C. Briens, "Continuous on-line measurement of solid moisture content during fluidized bed drying using triboelectric probes," *Powder Technol.* **181,** 169–177 (2008).

[29] G. Chaplin, T. Pugsley, and C. Winters, "Application of chaos analysis to pressure fluctuation data from a fluidized bed dryer containing pharmaceutical granule," *Powder Technol.* **142,** 110–120 (2004).

[30] L. de Martin, K. van der Dries, and J. R. van Ommen, "Comparison of three different methodologies of pressure signal processing to monitor fluidized-bed dryers/granulators," *Chem. Eng. J.* **172,** 487–499 (2011).

[31] D. Vervloet, J. Nijenhuis, and J. R. van Ommen, "Monitoring a lab-scale fluidized bed dryer: A comparison between pressure transducers, passive acoustic emissions and vibration measurements," *Powder Technol.* **197,** 36–348 (2010).

[32] M. Wormsbecker and T. Pugsley, "The influence of moisture on the fluidization behaviour of porous pharmaceutical granule," *Chem. Eng. Sci.* **63,** 4063–4069 (2008).

[33] M. Wormsbecker, T. Pugsley, and H. Tanfara, "Interpretation of the hydrodynamic behaviour in a conical fluidized bed dryer," *Chem. Eng. Sci.* **64,** 1739–1746 (2009).

[34] J. Johansson, M. Cauchi, and M. Sundgren, "Multiple fiber-optic dual-beam UV/Vis system with application to dissolution testing," *J. Pharm. Bio. Anal.* **29,** 469–476 (2002).

[35] X. Lu, R. Lozano, and P. Shah, "In-situ dissolution testing using UV fiber optic probes and intruments," *Dissolution Technol.* **10,** 6–15 (2003).

[36] H. Bohets, K. Vanhoutte, R. De Maesschalck, P. Cockaerts, B. Vissers, and L. J. Nagels, "Development of in situ ion selective sensors for dissolution," *Anal. Chim. Acta* **581,** 181–191 (2007).

[37] K. Peeters, R. De Maesschalck, H. Bohets, K. Vanhoutte, and L. Nagels, "In situ dissolution testing using potentiometric sensors," *Eur. J. Pharm. Sci.* **34,** 243–249 (2008).

[38] G. Bai, P. M. Armenante, and R. V. Plank, "Experimental and computational determination of blend time in USP dissolution testing apparatus II," *J. Pharm. Sci.* **96,** 3072–3086 (2007).

[39] Y. Roggo, P. Chalus, L. Maurer, C. Lema-Martinez, A. Edmond, and N. Jent, "A review of near infrared spectroscopy and chemometrics in pharmaceutical technologies," *J. Pharm. Biomed. Anal.* **44,** 683–700 (2007).

[40] P. J. Holden, M. Wang, R. Mann, F. J. Dickin, and R. B. Edwards, "Imaging stirred-vessel macromixing using electrical resistance tomography," *AlChE J.* **44,** 780–790 (1998).

[41] M. Wang, A. Dorward, D. Vlaev, and R. Mann, "Measurements of gas-liquid mixing in a stirred vessel using electrical resistance tomography (ERT)," *Chem. Eng. J.* **77,** 93–98 (2000).

[42] S. J. Stanley, R. Mann, and K. Primrose, "Tomographic imaging of fluid mixing in three dimensions for single-feed semi-batch operation of a stirred vessel," *Trans. IChemE., Part A* **80,** 903–909 (2002).

[43] H. S. Tapp, A. J. Peyton, E. K. Kemsley, and R. H. Wilson, "Chemical engineering applications of electrical process tomography," *Sens. Actuators B* **92,** 17–24 (2003).

[44] F. Ricard, C. Brechtelsbauer, X. Y. Xu, and C. J. Lawrence, "Monitoring of multiphase pharmaceutical processes using electrical resistance tomography," *Trans. IChemE., Part A* **83,** 794–805 (2005).

[45] J. Kourunen, R. Käyhkö, J. Matula, J. Käyhkö, M. Vauhkonen, and L. M. Heikkinen, "Imaging of mixing of two miscible liquids using electrical impedance tomography and linear impedance sensor," *Flow Meas. Instrum.* **19,** 391–396 (2008).

[46] M. A. Bennett and R. A. Williams, "Monitoring the operation of an oil/water separation using impedance tomography," *Minerals Eng.* **17,** 605–614 (2004).

[47] A. J. Jaworski and T. Dyakowski, "Measurement of oil-water separation dynamics in primary separation systems using distributed capacitance sensors," *Flow Meas. Instrum.* **16,** 113–127 (2005).

[48] J. A. Gutierrez-Gnecchi and E. Marroquin-Pineda, "Control of a pilot-scale, solid-liquid separation plant using electrical impedance tomography measurements," *Part. Part. Syst. Charact.* **25,** 306–313 (2008).

[49] A. Y. Nooralahiyan and B. S. Hoyle, "Three-component tomographic flow imaging using artificial neural network reconstruction," *Chem. Eng. Sci.* **52,** 2139–2148 (1997).

[50] T. Dyakowski, R. B. Edwards, C. G. Xie, and R. A. Williams, "Application of capacitance tomography to gas-solid flows," *Chem. Eng. Sci.* **52,** 2099–2110 (1997).

[51] T. Dyakowski, L. F. C. Jeanmeure, and A. J. Jaworski, "Applications of electrical tomography for gas-solids and liquid-solids flows - a review," *Powder Technol.* **112,** 174–192 (2000).

[52] W. Warsito and L.-S. Fan, "ECT imaging of three-phase fluidized bed based on three-phase capacitance model," *Chem. Eng. Sci.* **58,** 823–832 (2003).

[53] I. Ismail, J. C. Gamio, S. F. A. Bukhari, and W. Q. Yang, "Tomography for multi-phase flow measurement in the oil industry," *Flow Meas. Instrum.* **16,** 145–155 (2005).

[54] F. Wang, Q. Marashdeh, L.-S. Fan, and W. Warsito, "Electrical capacitance volume tomography: design and applications," *Sensors* **10,** 1890–1917 (2010).

[55] K. Zhu, S. M. Rao, C.-H. Wang, and S. Sundaresan, "Electrical capacitance tomography measurements on vertical and inclined pneumatic conveying of granular solids," *Chem. Eng. Sci.* **58,** 4225–4245 (2003).

[56] B. H. Brown, "Electrical impedance tomography (EIT): a review," *J. Med. Eng. Technol.* **27,** 97–108 (2003).

[57] Y. Zou and Z. Guo, "A review of electrical impedance techniques for breast cancer detection," *Med. Eng. Phys.* **25,** 79–90 (2003).

[58] J. A. Victorino, J. B. Borges, V. N. Okamoto, G. F. J. Matos, M. R. Tucci, M. P. R. Caramez, H. Tanaka, F. S. Sipmann, D. C. B. Santos, B. C. S. V., C. R. R. Carvalho, and M. B. P.

Amato, "Imbalances in regional lung ventilation: A validation study on electrical impedance tomography," *Am. J. Respir. Crit. Care Med.* **169,** 791–800 (2004).

[59] A. Samouëlian, I. Cousin, A. Tabbagh, A. Bruand, and G. Richard, "Electrical resistivity survey in soil science: a review," *Soil Till. Res.* **83,** 173–193 (2005).

[60] P. Soupios, I. Papadopoulos, M. Kouli, I. Georgaki, F. Vallianatos, and E. Kokkinou, "Investigation of waste disposal areas using electrical methods: a case study from Chania, Crete, Greece," *Environ. Geol.* **51,** 1249–1261 (2006).

[61] B. Heincke, T. Günther, E. Dalsegg, J. S. Rønning, G. V. Ganerød, and H. Elvebakk, "Combined three-dimensional electric and seismic tomography study on the Åknes rockslide in western Norway," *J. Appl. Geophys.* **70,** 292–306 (2010).

[62] K. Karhunen, A. Seppänen, A. Lehikoinen, M. P. J. M., and J. P. Kaipio, "Electrical resistance tomography imaging of concrete," *Cem. Concr. Res.* **40,** 137–145 (2010).

[63] F. Ricard, C. Brechtelsbauer, Y. Xu, C. Lawrence, and D. Thompson, "Development of an electrical resistance tomography reactor for pharmaceutical processes," *Can. J. Chem. Eng.* **83,** 11–18 (2005).

[64] H. Wang, W. Yang, I. Proctor, J. Taylor, A. Marr, and T. Page, "Online monitoring and flow regime identification of fluidised bed drying and granulation processes," in *IEEE International Workshop on Imaging Systems and Techniques* (2009), pp. 247–252.

[65] G. Chaplin, T. Pugsley, L. van der Lee, A. Kantzas, and C. Winters, "The dynamic calibration of an electrical capacitance tomography sensor applied to the fluidized bed drying of pharmaceutical granule," *Meas. Sci. Technol.* **16,** 1281–1290 (2005).

[66] G. Chaplin and T. Pugsley, "Application of electrical capacitance tomography to the fluidized bed drying of pharmaceutical granule," *Chem. Eng. Sci.* **60,** 7022–7033 (2005).

[67] H. G. Wang, W. Q. Yang, P. R. Senior, R. S. Raghavan, and S. R. Duncan, "Investigation of batch fluidized-bed drying by mathematical modeling, CFD simulation and ECT measurement," *AlChE J.* **54,** 427–444 (2008).

[68] H. G. Wang, P. R. Senior, R. Mann, and W. Q. Yang, "Online measurement and control of solids moisture in fluidized bed dryers," *Chem. Eng. Sci.* **64,** 2893–2902 (2009).

[69] H. G. Wang and W. Q. Yang, "Measurement of fluidised bed dryer by different frequency and different normalisation methods with electrical capacitance tomography," *Powder Technol.* **199,** 60–69 (2010).

[70] M. Takei, T. Zhao, and K. Yamane, "Measurement of particle concentration in powder coating process using capacitance computed tomography and wavelet analysis," *Powder Technol.* **193,** 93–100 (2009).

[71] W. Q. Yang and L. Peng, "Image reconstruction algorithms for electrical capacitance tomography," *Meas. Sci. Technol.* **14,** R1–R13 (2003).

[72] Q. Marashdeh, L.-S. Fan, B. Du, and W. Warsito, "Electrical capacitance tomography - a perspective," *Ind. Eng. Chem. Res.* **47,** 3708–3719 (2008).

[73] D. Watzenig and C. Fox, "A review of statistical modelling and inference for electrical capacitance tomography," *Meas. Sci. Technol.* **20,** 052002 (2009).

[74] M. Cheney, D. Isaacson, and J. C. Newell, "Electrical impedance tomography," *SIAM Rev.* **41,** 85–101 (1999).

[75] L. Borcea, "Electrical impedance tomography," *Inverse Problems* **18,** R99–R136 (2002).

[76] W. R. B. Lionheart, "EIT reconstruction algorithms: pitfalls challenges and recent developments," *Physiol. Meas.* **25,** 125–142 (2004).

[77] A. F. Kip, *Fundamentals of electricity and magnetism*, 2nd ed. (McGraw-Hill Book Company, 1969).

[78] R. Banasiak, R. Wajman, D. Sankowski, and M. Soleimani, "Three-dimensional nonlinear inversion of electrical capacitance tomography data using a complete sensor model," *Progress In Electromagnetics Research, PIER* **100,** 219–234 (2010).

[79] Q. Marashdeh, *Advances in electrical capacitance tomoraphy*, PhD thesis (Ohio State University, 2006).

[80] M. Neumayer, H. Zangl, D. Watzenig, and A. Fuchs, Chap Current reconstruction algorithms in electrical capacitance tomography in *New developments and applications in sensing technology* (Springer, 2011).

[81] P. J. Vauhkonen, M. Vauhkonen, T. Savolainen, and J. P. Kaipio, "Three-dimensional electrical impedance tomography based on complete electrode model," *IEEE Trans. Biomed. Eng.* **46,** 1150–1160 (1999).

[82] E. Somersalo, M. Cheney, and D. Isaacson, "Existence and uniqueness for electrode models for electric current computed tomography," *SIAM J. Appl. Math.* **52,** 1023–1040 (1992).

[83] K.-S. Cheng, D. Isaacson, J. C. Newell, and D. G. Gisser, "Electrode models for electric current computed tomography," *IEEE Trans. Biomed. Eng.* **36,** 918–924 (1989).

[84] T. Vilhunen, J. P. Kaipio, P. J. Vauhkonen, T. Savolainen, and M. Vauhkonen, "Simultaneous reconstruction of electrode contact impedances and internal electrical properties: I. Theory," *Meas. Sci. Technol.* **13,** 1848–1854 (2002).

[85] L. M. Heikkinen, T. Vilhunen, R. M. West, and M. Vauhkonen, "Simultaneous reconstruction of electrode contact impedances and internal properties: II. Laboratory experiments," *Meas. Sci. Technol.* **13,** 1855–1861 (2002).

[86] N. Polydorides, *Image reconstruction algorithms for soft-field tomography*, PhD thesis (University of Manchester Institute of Science and Technology, 2002).

[87] P. J. Vauhkonen, *Image reconstruction in three-dimensional electrical impedance tomography*, PhD thesis (University of Kuopio, 2004).

[88] C. Tibirna, D. Edouard, A. Fortin, and F. Larachi, "Usability of ECT for quantitative and qualitative characterization of trickle-bed flow dynamics subject to filtration conditions," *Chem. Eng. Process.* **45,** 538–545 (2006).

[89] M. Vauhkonen, P. A. Karjalainen, and J. P. Kaipio, "A Kalman filter approach to track fast impedance changes in electrical impedance tomography," *IEEE Trans. Biomed. Eng.* **45,** 486–493 (1998).

[90] K. Y. Kim, B. S. Kim, M. C. Kim, Y. J. Lee, and M. Vauhkonen, "Image reconstruction in time-varying electrical impedance tomography based on the extended Kalman filter," *Meas. Sci. Technol.* **12,** 1032–1039 (2001).

[91] K. Y. Kim, S. I. Kang, M. C. Kim, S. Kim, Y. J. Lee, and M. Vauhkonen, "Dynamic image reconstruction in electrical impedance tomography with known internal surfaces," *IEEE Trans. Magn.* **38,** 1301–1304 (2002).

[92] B. S. Kim, K. Y. Kim, T.-J. Kao, J. C. Newell, D. Isaacson, and G. J. Saulnier, "Dynamic electrical impedance imaging of a chest phantom using the Kalman filter," *Physiol. Meas.* **27,** S81–S91 (2006).

[93] A. Seppänen, *State estimation in process tomography*, PhD thesis (University of Kuopio, 2005).

[94] A. Seppänen, L. Heikkinen, T. Savolainen, A. Voutilainen, E. Somersalo, and J. P. Kaipio, "An experimental evaluation of state estimation with fluid dynamical models in process tomography," *Chem. Eng. J.* **127,** 23–30 (2007).

[95] M. Soleimani, M. Vauhkonen, W. Yang, P. A., B. S. Kim, and X. Ma, "Dynamic imaging in electrical capacitance tomography and electromagnetic induction tomography using a Kalman filter," *Meas. Sci. Technol.* **18,** 3287–3294 (2007).

[96] J. L. Mueller, S. Siltanen, and D. Isaacson, "Direct reconstruction algorithm for electrical impedance tomography," *IEEE Trans. Med. Imag.* **21,** 555–559 (2002).

[97] E. K. Murphy, J. L. Mueller, and J. C. Newell, "Reconstruction of conductive and insulating targets using the D-bar method on an elliptical domain," *Physiol. Meas.* **28,** S101–S114 (2007).

[98] K. Knudsen, M. Lassas, J. L. Mueller, and S. Siltanen, "Regularized D-bar method for the inverse conductivity problem," *Inverse Probl. Imaging* **3,** 599–624 (2009).

[99] J. Kaipio and E. Somersalo, *Statistical and computational inverse problems* (Springer, 2005).

[100] D. Calvetti and E. Somersalo, *Introduction to Bayesian scientific computing: Ten lectures on subjective computing* (Springer, 2007).

[101] J. P. Kaipio, V. Kolehmainen, E. Somersalo, and M. Vauhkonen, "Statistical inversion and Monte Carlo sampling methods in electrical impedance tomography," *Inverse Problems* **16,** 1487–1522 (2000).

[102] V. Kolehmainen, *Novel approaches to image reconstruction in diffusion tomography*, PhD thesis (University of Kuopio, 2001).

[103] A. Nissinen, L. M. Heikkinen, and J. P. Kaipio, "The Bayesian approximation error approach for electrical impedance tomography," *Meas. Sci. Technol.* **19,** 015501 (2008).

[104] A. Lipponen, A. Seppänen, and J. P. Kaipio, "Reduced-order estimation of nonstationary flows with electrical impedance tomography," *Inverse Problems* **26,** 074010 (2010).

[105] A. Nissinen, V. Kolehmainen, and J. P. Kaipio, "Reconstruction of domain boundary and conductivity in electrical impedance tomography using the approximation error approach," *Int. J. Uncertainty Quantification* **1,** 203–222 (2011).

[106] A. Lipponen, A. Seppänen, and J. P. Kaipio, "Nonstationary approximation error approach to imaging of three-dimensional pipe flow: experimental evaluation," *Meas. Sci. Technol.* **22,** 104013 (2011).

[107] P. Williams and T. York, "Integrated intelligent electrodes for electrical capacitance tomography," *IEE Digest* **1996,** 15–15 (1996).

[108] V. Kolehmainen, M. Vauhkonen, P. A. Karjalainen, and J. P. Kaipio, "Assessment of errors in static electrical impedance tomography with adjacent and trigonometric current patterns," *Physiol. Meas.* **18,** 289–303 (1997).

[109] W. R. B. Lionheart, J. P. Kaipio, and C. N. McLeod, "Generalized optimal current patterns and electrical safety in EIT," *Physiol. Meas.* **22,** 85–90 (2001).

[110] J. P. Kaipio, A. Seppänen, E. Somersalo, and H. Haario, "Posterior covariance related optimal current patterns in electrical impedance tomography," *Inverse Problems* **20,** 919–936 (2004).

[111] A. Adler, P. O. Gaggero, and Y. Maimaitijiang, "Adjacent stimulation and measurement patterns considered harmful," *Physiol. Meas.* **32,** 731–744 (2011).

[112] G. E. Fasching and N. S. Smith, "A capacitive system for three-dimensional imaging of fluidized beds," *Rev. Sci. Instrum.* **1991,** 2243–2251 (1991).

[113] S. M. Huang, X. C. G., R. Thorn, D. Snowden, and M. S. Beck, "Design of sensor electronics for electrical capacitance tomography," *IEE Proc.-G.* **139,** 83–88 (1992).

[114] H. Wegleiter, A. Fuchs, G. Holler, and B. Kortschak, "Development of a displacement current-based sensor for electrical capacitance tomography applications," *Flow. Meas. Instrum.* **19,** 241–250 (2008).

[115] W. Q. Yang, "Hardware design of electrical capacitance tomography systems," *Meas. Sci. Technol.* **7,** 225–232 (1996).

[116] H. Yan, F. Q. Shao, H. Xu, and S. Wang, "Three-dimensional analysis of electrical capacitance tomography sensing fields," *Meas. Sci. Technol.* **10,** 717–725 (1999).

[117] W. Q. Yang, "Further improvements in an ac-based capacitance tomography system," *Rev. Sci. Instrum.* **72,** 3902–3907 (2001).

[118] R. D. Cook, G. J. Saulnier, D. G. Gisser, J. C. Goble, J. C. Newell, and D. Isaacson, "ACT3: a high-speed, high-precision electrical impedance tomograph," *IEEE Trans. Biomed. Eng.* **41,** 713–722 (1994).

[119] J. Kourunen, T. Savolainen, A. Lehikoinen, M. Vauhkonen, and L. M. Heikkinen, "Suitability of a PXI platform for an electrical impedance tomography system," *Meas. Sci. Technol.* **20,** 015503 (2009).

[120] T. I. Oh, E. J. Woo, and D. Holder, "Multi-frequency EIT system with radially symmetric architecture: KHU Mark1," *Physiol. Meas.* **28,** S183–S196 (2007).

[121] T. Savolainen, J. P. Kaipio, P. A. Karjalainen, and M. Vauhkonen, "An electrical impedance tomography measurement system for experimental use," *Rev. Sci. Instrum.* **67,** 3605 (1996).

[122] A. J. Wilson, P. Milnes, A. R. Waterworth, R. H. Smallwood, and B. H. Brown, "Mk3.5: a modular, multi-frequency successor to the Mk3a EIS/EIT system," *Physiol. Meas.* **22,** 49–54 (2001).

[123] A. J. Wilkinson, E. W. Randall, T. M. Long, and A. Collins, "The design of an ERT system for 3D data acquisition and a quantitative evaluation of its performance," *Meas. Sci. Technol.* **17,** 2088–2096 (2006).

[124] M. Wang, Y. Ma, N. Holliday, Y. Dai, R. A. Williams, and G. Lucas, "A high-performance EIT system," *IEEE Sensors J.* **5,** 289–299 (2005).

[125] A. J. Jaworski and G. T. Bolton, "The design of an electrical capacitance tomography sensor for use with media of high dielectric permittivity," *Meas. Sci. Technol.* **11,** 743–757 (2000).

[126] A. M. Olmos, J. A. Primicia, and J. L. F. Marron, "Simulation design of electrical capacitance tomography sensors," *IET Sci. Meas. Technol.* **1,** 216–223 (2007).

[127] W. Yang, "Design of electrical capacitance tomography sensors," *Meas. Sci. Technol.* **21,** 042001 (2010).

[128] M. Wang, F. J. Dickin, and R. A. Williams, "Modelling and analysis of electrically conducting vessels and pipelines in electrical resistance process tomography," *IEE Proc.-Sci. Meas. Technol.* **142,** 313–322 (1995).

[129] V. Wiesendorf and J. Werther, "Capacitance probes for solids volume concentration and velocity measurements in industrial fluidized bed reactors," *Powder Technol.* **110,** 143–157 (2000).

[130] G. T. Bolton, C. H. Qui, and M. Wang, "A novel electrical tomography sensor for monitoring the phase distribution in industrial reactors," *Proc. Fluid Mixing 7* (2002).

[131] N. Polydorides and W. R. B. Lionheart, "A Matlab toolkit for three-dimensional electrical impedance tomography: a contribution to the Electrical Impedance and Diffuse Optical Reconstruction Software project," *Meas. Sci. Technol.* **13,** 1871–1883 (2002).

[132] M. Vauhkonen, W. R. B. Lionheart, L. M. Heikkinen, P. J. Vauhkonen, and K. J. P., "A Matlab package for the EIDORS project to reconstruct two-dimensional EIT images," *Physiol. Meas.* **22,** 107–111 (2001).

[133] V. Rimpiläinen, S. Poutiainen, L. M. Heikkinen, T. Savolainen, M. Vauhkonen, and J. Ketolainen, "Monitoring of high-shear mixing and granulation with capacitive measurements and tomography," *6th World Congress on Industrial Process Tomography* 44-51 (2010).

[134] H. Leuenberger, M. Puchkov, E. Krausbauer, and G. Betz, "Manufacturing pharmaceutical granules: Is the granulation end-point a myth?," *Powder Technol.* **189,** 141–148 (2009).

[135] W. Q. Yang, A. Chondronasios, S. Nattrass, V. T. Nguyen, M. Betting, I. Ismail, and H. McCann, "Adaptive calibration of a capacitance tomography system for imaging water droplet distribution," *Flow Meas. Instrum.* **15,** 249–258 (2004).

[136] J. W. Moore and H. H. Flanner, "Mathematical comparison of dissolution profiles," *Pharm. Tech.* **20,** 64–74 (1996).

[137] S. J. R. Simons, X. Ni, H. T. Tabe, R. M. West, and R. A. Williams, "Reduction of tomographic data for use in the control of multiphase processes," *Chem. Eng. Comm.* **175,** 99–115 (1999).

[138] M. Stasiak, J. Sikora, S. F. Filipowicz, and K. Nita, "Principal component analysis and artificial neural network approach to electrical impedance tomography problems approximated by multi-region boundary element method," *Eng. Anal. Boundary Elem.* **31,** 713–720 (2007).

[139] H. Wang and W. Yang, "Scale-up of an electrical capacitance tomography sensor for imaging pharmaceutical fluidized beds and validation by computational fluid dynamics," *Meas. Sci. Technol.* **22,** 104015 (2011).

[140] L. M. Heikkinen, M. Vauhkonen, T. Savolainen, and J. P. Kaipio, "Modelling of internal structures and electrodes in electrical process tomography," *Meas. Sci. Technol.* **12,** 1012–1019 (2001).

[141] X. Y. Dong and S. Q. Guo, "Modelling an electrical capacitance tomography sensor with internal plate electrode," *International Conference on Test and Measurement* 160-163 (2009).

Ville Rimpiläinen

Electrical tomography imaging in pharmaceutical processes

Electrical capacitance tomography (ECT) and electrical impedance tomography (EIT) are imaging modalities which can be used to characterize electrical properties inside different processing vessels. In this thesis, ECT and EIT have been applied in monitoring of three common pharmaceutical unit processes: high-shear granulation, fluidized-bed drying and dissolution testing. The thesis describes various technical means how to implement the imaging modalities, studies the applicability and shows how to generate appropriate process monitoring signals.

UNIVERSITY OF
EASTERN FINLAND

Publications of the University of Eastern Finland
Dissertations in Forestry and Natural Sciences

ISBN 978-952-61-0777-6